Title: Interphase misorientation as a tool to study metamorphic reactions and crystallization in geological materials
Manuscript Number: 7902R
Authors: Luiz Morales, ETH Zürich

Revision 1 –

Word count: 10988

Interphase misorientation as a tool to study metamorphic reactions and crystallization in geological materials

Luiz F. G. Morales [a,b]

[a] Scientific Center for Optical and Electron Microscopy (ScopeM), ETH Zürich, Otto-Stern-Weg 3, 8093, Zürich.

[b] Geological Institute, Department of Earth Sciences, ETH Zürich, Sonneggstrasse 5, 8092 Zurich

Email: luiz.morales@scopem.ethz.ch

Abstract

Interphase boundaries are planar defects that separate two different minerals, which in general have different compositions and/or crystalline structures and may play an important role as a pathway for fluids in rocks and affect their physical properties. For the proper characterization of interphase boundaries, one needs to define the misorientation between adjacent grains and the orientation of the grain boundary plane, but the analysis performed here are only limited to the misorientation characterization and the trace of the interphase boundary. Although the determination of possible orientation relationships between the two adjacent phases is routinely performed by selected area electron diffraction in the transmission electron microscope, this method lacks statistical representativeness. With the advent of techniques like electron backscatter diffraction (EBSD), it is possible to calculate orientation relationships not only in single pairs of crystals, but in full thin sections, and not limited to single phases, but also between different minerals.

The interphasee misorientation is calculated from two orientations of two adjacent crystals of different phases. A set of single misorientations is then used to calculate the misorientation distribution function (MDF), from where it is possible to identify a maximum, and their crystallographic interpretation. If we then know the misorientation and the unit cell parameters of the individual phases, the crystallographic relationships between them can be described with the pairs of parallel crystallographic planes and the pairs of crystallographic directions. We present examples of the use of interphase misorientation analysis on the transformation of calcite-aragonite, olivine-antigorite, magnetite-hematite, and on the study of orientation relationships between plagioclase-olivine-ilmenite in mid-ocean ridges gabbros (ODP Hole 735).

Keywords

Interphase misorientation; EBSD; orientation relationships; phase transformation

INTRODUCTION

Polycrystalline material such as rocks, metals and ceramics are made of different grains with different crystal orientations. Where those grains meet each other, there is normally an interatomic mismatch between the lattices of the two adjacent crystals, which are called grain or phase boundaries. Grain and phase boundaries are a very important part of the microstructure of rocks because they are high diffusivity paths for both fluids and solid-state diffusion. They play an important role on the rheology of rocks and influence petrophysical properties, such as strength of rocks, resistance to cracking and permeability. As grain and phase boundaries are relatively disordered structures, they can accommodate large amounts of impurities, which may influence, for example, boundary migration

Grain boundaries are interfaces that separate grains of the same phase (e.g. quartz grain boundaries), whereas phase boundaries separate grains of different compositions and/or structure (e.g. quartz-feldspar or calcite-aragonite phase boundaries). The structure and energy of grain boundaries are defined by the

misorientation of the two neighboring grains and the orientation of the boundary plane itself. To fully define a grain boundary, one must define 5 variables related to the grain boundary misorientation angle, misorientation axes and the orientation of the interface itself. Standard classification of grain boundaries distinguishes two end members, named tilt and twist boundaries. In tilt boundaries, the rotation axis to bring the lattices of two neighboring crystals into overlap is parallel to the interface plane, whereas in twist boundaries, the rotation axis is normal to the interface, and pretty much all grain boundaries lie in between these two end-members. Grain boundaries are also classified according to the misorientation angle. Adjacent grain boundaries with less than 10° misorientation between neighbor grains are said to be low angle grain boundaries, while neighboring grain boundaries with higher degrees of misorientations re classified as high angle grain boundaries. In deformed materials, low angle grain boundaries are commonly associated with array of aligned dislocations along a certain plane (forming in this case a "subgrain"), but it is important to note that low angle grain boundaries are very important in biomineralization and have nothing to do with intracrystalline defects.

Phase boundaries on the other hand are classified according to the degree of mismatch between the lattices of the two phases along the interface (e.g. Sutton and Baluffi, 1995; Porter and Easterling, 1992). In coherent (or commensurate) phase boundaries (Fig. 1), the two neighbor crystals match perfectly along the interface, and the interfacial plane has the same atomic configuration in both phases. An important aspect of the coherency definition is that the crystallographic plane comprising the phase boundary does not need to be the same in the different phases, but an orientation relationship between the two grains needs to be satisfied. This can be described by a Burgers orientation relationship that specifies a pair of parallel planes and directions, i.e., $(hkl)_{phase\ A} \parallel (hkl)_{phase\ B}$ and $[uvw]_{phaseA} \parallel [uvw]_{phaseB}$ for the general case of single planes and directions. In order to keep the interface coherent, small differences in the lattice parameters between the two phases can be accommodated by elastic strains on both sides separated by the interface. Such an effect reduces the interface energy at the expense of increasing the internal energy of both phases adjacent to the interface. As such, elastic straining in order to force a perfect coherency only occurs if the

interface is strong, if the mismatch is small and if the grain size is small. Although the structure at the interface is perfect, the interfacial energy at the boundary is quite variable, but depends essentially on the composition of the phases separated by the interface. In semi-coherent (or discommensurate) phase boundaries, the elastic strain described previously becomes too large and the lattice mismatch is accommodated by an array of misfit dislocations that do not create long-range strain fields. The total energy of semi-coherent phase boundaries results from both compositional and structural components. In incoherent (or incommensurate) phase boundaries, the different lattices of the two phases at the interface prevents the good matching at the phase boundary, leading to a more disorder structure, similar to those observed in high-angle grain boundaries. The surface energy of both grain and phase boundaries are function of the misorientation angle, and it is known from the material science literature that during deformation, grain boundaries in metals tend to rotate to minimize such energy, leading to the development of grain boundaries with specific misorientation angles.

Grain boundaries on common minerals such as quartz, olivine and calcite are relatively well understood in various scales (e.g. McLaren 1986; Faul and Fitz-Gerald 1999; Fliervoet et al., 1999; Wheeler at al. 2001; Bestmann et al. 2004; Lloyd et al. 2004, Hiraga et al. 2004; Wenk et al. 2011, Menegon et al. 2011; Kilian et al. 2011; Krühl et al. 2013 and others). In olivine, for example, special grain boundaries have even been characterized in terms of grain boundary character distribution (Marquardt et al. 2015) and in terms of grain boundary energies (Duyster and Stöckert, 2001). However, although "real" rocks are mostly composed of two or more phases, our understanding of phase boundaries between different minerals is very scarce and predominantly studied at the nanometric scale, with most observations performed in transmission electron microscopes (TEM - e.g. Boudier et al. 2010; Plümper et al. 2011; Obata and Osawa 2011; Marti et al. 2018). Although this is a very powerful tool to investigate interphase boundaries particularly due to its angular resolution (interphase orientations can be determined up to a precision of 0.1°), it has a very limited statistical representativeness, where an individual TEM lamella will show at most a few interfaces. However, the TEM is not the only technique available to study orientation

relationships between different phases, and any technique involving local diffraction of an electron beam by the crystalline structure of the phases separated by the interface will allow us to calculate the orientation relationship. Here it is proposed to use orientation maps generated via electron backscatter diffraction (EBSD) in a scanning electron microscope (SEM) to calculate the interphase misorientation angle/axis and from these data to calculate potential orientation relationships. . It is important to clarify here that the "orientation relationships" described here have a different meaning to that described in crystallography, where there is partial/total coincidence between the lattices of the two materials separated by an interface. Here I use the term is a more "loose" way, to described that, in certain cases, two different minerals may show some degree of parallelism along certain interfaces without necessarily sharing the same lattice along the interface. Advantages of this method include (i) the higher statistical representativeness of the data, (ii) the potential to calculate the misorientation angle-axis pair of any pair of mineral phases, (iii) the potential to plot phase boundaries of different misorientation angles in the map, and highlight those which have special misorientation angles/axis and even possible orientation relationships and (iv) to use EBSD results and subsequent calculations tackle more detailed studies of specific interphase boundaries on the TEM scale, preparing TEM lamellae using target preparation with focused ion beam methods for example. Here I present 4 examples of interphase misorientations and interphase orientation relationships between olivine-antigorite from a serpentinite, calcite-aragonite from high P-T experiments, magnetite-hematite from an undeformed iron ore, and plagioclase-ilmenite relationships from a mid-ocean ridge gabbro. The results are presented in terms of interphase misorientation angles, axes, and plotted directly in the EBSD maps. In order to facilitate the use of this method, a MATLAB script to be used in the MTEX toolbox from Hielscher and Schaeben (2008) is provided as supplementary material.

INTERPHASE BOUNDARY MISORIENTATIONS

Interphase boundary misorientations calculations are relatively new in Earth and Material Sciences. For instance, McNamara et al. (2012) explored interphase misorientation relationships on the study of crystallographic preferred orientation (CPO) development of barroisite due to mimetic growth at the expense of glaucophane and omphacite. Later, Morales et al. (2018) use the interphase angle/axis pair on the study of olivine-antigorite transformation relationships, where they reported two new orientation relationships never described in the literature. We should briefly step back and look the concept of intraphase misorientation, where a complete overview of this topic is given by Wheeler et al. (2001).

Crystal orientations $\boldsymbol{g}$ as determined via EBSD and consistent with the definitions of MTEX can be described as passive rotations $\boldsymbol{r}$ to bring the coordinates from the crystal reference into coordinates in the sample reference frame. Both reference frames are right-handed, the three axes are orthogonal to each other, and both share a common origin for the sake of simplicity (note however that in some cases, the crystal reference frames might not be orthogonal). The rotation angle is always positive if the rotation is counterclockwise when viewed along the rotation axis towards the origin. Using the definitions of Krakow et al. (2017), if we define the specimen reference frame as $\boldsymbol{s}$ and the crystal reference frame as $\boldsymbol{e}$, the rotation has to satisfy

$$r = \boldsymbol{G}.e \qquad (1)$$

where $r=(x,y,z)$ in specimen coordinates and $e=(e_1,e_2,e_3)$, in crystal coordinates. This equation states that a vector r can be transformed into a vector e by an operation $\boldsymbol{G}$, which is a matrix operation.

The misorientation angle in an EBSD map is the angle necessary to bring two adjacent objects of this map (i.e. two neighbor pixels, or two neighbor grains) into overlap, whereas the misorientation axis is the axis in which this rotation needs to occur to bring the lattices of the two objects into parallelism. These misorientations $\boldsymbol{M}$ are also passive rotations, but in this case between two crystals reference frames, where

the two crystal normally have two different orientations (g_1 & g_2). The misorientation $\boldsymbol{M}$ between these two crystals transforms the crystal coordinates $\boldsymbol{c_1}$ into crystal coordinates $\boldsymbol{c_2}$, as follows (e.g. Krakow et al., 2017)

$$\boldsymbol{M}=\boldsymbol{g_2^{-1}}.\boldsymbol{g_1} \quad (2)$$

and

$$\boldsymbol{M}\boldsymbol{c_1} = \boldsymbol{g_2^{-1}}\boldsymbol{g_1}\boldsymbol{c_1} = \boldsymbol{g_2^{-1}}\boldsymbol{r} = \boldsymbol{c_2} \quad (3)$$

When dealing with one single phase, the lattice parameters for the adjacent objects are the same, and so the misorientation axis can be defined by a number of symmetrically equivalent axis/angle pair combinations that are directly dependent on the symmetry of the studied phase. In the case of two neighbor plagioclase (triclinic) grains, there is only one set of misorientation angle/axis capable to bring the lattices of these two grains into overlap, while in the case of magnetite or garnet (cubic minerals), there are 24 different possibilities (Mainprice et al. 1993; Lloyd et al. 1997; Wheeler et al. 2001). In the case of olivine (orthorhombic) there will be less than 24 possibilities Due to this large number of possibilities in non-triclinic phases, the current convention is to adopt the pair with the minimum misorientation angle of the equivalent rotations (e.g. Morawiec et al., 1995; Wheeler et al. 2001).

On the other hand, when dealing with the misorientation between two phases that belong to different crystallographic systems, the reference misorientation is not unique. Because of that, and due to the fact, that in most cases we will deal with phases of different symmetries, the asymmetric domain for the misorientation axis plots is not ‘fundamental’. That implies that the shape and form of misorientation angle/axis distribution depends on the choice of reference misorientation. If we consider the example of olivine (orthorhombic) and antigorite (monoclinic), the fundamental region requires the entire hemisphere

due to the combination of these two different symmetries. In this case, we must define in relation to which crystal reference frame we will plot the misorientation axes. In the case of phase transformations, it makes sense to use the parent phase reference frame, but if one suspects that a different interphase orientation relationship can be deduced from the interphase misorientation data, one has to examinate the misorientation axes plot using also the daughter phase reference frame.

In most of the studies dealing with misorientations, fundamental zones are based on Rodrigues-Frank parameters (e.g. Morawiec, 1997), but in MTEX this construction is based on quaternion geometry (see Krakow et al., 2017 for details). The definition of a particular fundamental zone depends on the alignment of crystal axes and the order in which the symmetry operators are combined for the misorientation calculations. These fundamental zones are calculated by selecting, in a family of symmetrically related equivalent points, the ones with the smallest angle of rotation. If then multiple points have the same distance from the origin, the choice is made based on the direction of the rotation axis.

Crystallographic point groups control the symmetry operations related to misorientations. If we have misorientation $\boldsymbol{M}$ relating point groups S_1 and S_2 with crystal coordinate systems c_1 and c_2, and using the equation (3), we can write the following expression

$$\boldsymbol{M}=s_2\boldsymbol{M}s_1,\ s_1 \in S_1,\ s_2 \in S_2 \qquad (4)$$

Here we use the smallest unique rotation angle (disorientation angle) and the axis of rotation within the inverse pole figure sector that correspond to the point group common to both symmetries, fulfilling the relation SC =S1 ∩ S2. The fundamental zones for all possible combinations of proper point group symmetry operations are presented in Krakow et al. (2017), but for the sake of simplicity, all the misorientation axes plots are presented in inverse pole figures resulting from those combinations.

DESCRIPTION OF THE SAMPLES

To test the potential of misorientation analysis on the study of metamorphic reactions and magmatic processes, we have studied four different samples (one experimental and three natural). Three of these samples are known examples of phase transformations or crystallographically controlled metamorphic reactions and include (i) calcite-aragonite; (ii) olivine-antigorite and (iii) magnetite-hematite. In all those cases, the neighbouring phases that share a common boundary do not belong to the same crystallographic system. The fourth example is an oxide-rich gabbro coming from the Atlantis Bank (Indian Ocean), where I have tested all the possible pairs of 6 different minerals that compose this rock (plagioclase, diopside, olivine, ilmenite, magnetite and pargasite) and I found that plagioclase-olivine and plagioclase-ilmenite have specific misorientation angle/axis pairs that suggests that both olivine and ilmenite crystallized using specific plagioclase crystal planes as substrate..

Calcite - Aragonite phase transformation produced experimentally

The calcite-aragonite aggregated studied here (sample 010-SC-3-X) belong to the collection of deformation experiments performed by Sebastian Cionoiu during his PhD thesis at ETH Zürich, whose objective was to understand the effect of stress on mineral reactions (see thesis volume for sample preparation details). The calcite-aragonite phase transformation observed in this sample occurred under hydrostatic conditions (i.e. no axial load applied) under 1.6 GPa pressure and temperatures of 600°C for about 12 hours. In the studied sample, aragonite comprises about 15 % of the total aggregate and occurs predominantly wrapped around large calcite crystals, as if forming tails of recrystallized material (Fig. 4a). Calcite is heavily twinned and has some undulose extiction, but no clear subgrains or recrystallized grains, and no noticeable grain growth has been observed. Aragonite grain sizes vary from 3 µm to 12 µm and there is no clear evidence of crystal plasticity in this phase such as undulose extinction or subgrain walls.

Tremolite-chlorite-antigorite schist from Moses Rock (USA)

The sample of tremolite-chlorite-antigorite schist studied here (MR-1) was collected from the Moses Rock dike and was previously studied by Boudier et al. (2010) and Morales et al. (2013). The Moses rock dike belongs to the Navajo Volcanic Field (NVF) that is exposed in the central part of the Colorado Plateau, in the Four-Corners region, SW of USA. The Moses Rock dike belongs to kimberlitic and lamprophyric breccias that contain a large variety of mantle and lower crustal xenoliths of a variety of compositions (Smith, 1995, 2010). The mantle fragments, associated with the subduction of the Farallon slab, include metaperidotites rich in hydrous phases, jadeite clinopyroxenites and eclogites, spinel websterite and spinel lherzolites and were formed at depths between 50 and 150 km and temperatures ~900 °C according to clinopyroxene thermometry (Hunter and Smith, 1981),

Magnetite – hematite phase transformation

The magnetite-hematite studied here was collected in the Corrego do Feijão mine in the western part of the Quadrilátero Ferrífero, southeastern Brazil. This “iron quadrangle” lies within the Cauê formation of the Itabira group, a metasedimantary sequence of Archean/Paleoproterozoic ages that lies on the southern boundary of the São Francisco craton (Alkmin and Marshak, 1998). This sequence hosts large iron ore deposits in the form of itabirites and polycrystalline hematite with variable contents of magnetite. Deformation intensity and metamorphic conditions increases from east to west (Rosière et al., 2001), and the iron ores present a progressive enrichment of hematite in relation to magnetite towards the east. The studied sample is still relatively rich in magnetite and is composed approximately by 60 % magnetite and 40% hematite, with goethite occurring as alteration material.

Plagioclase-olivine and plagioclase-ilmenite from oxide gabbro from the Atlantis Bank

The Atlantis bank is an oceanic core complex that was exhumed by a large-scale detachment fault on the Southwest Indian Ridge (Karson and Lawrance 1997, Kelemen et al. 2007). Deformation in these rocks is localized along hypersolidus and HT shear zones, later overprinted by brittle faults of different scales, as detailed described by Miranda et al. 2010 and Allard et al. (2021). Here we studied oxide-rich gabbros that occur with higher frequency toward the top of the borehole and are interpreted to have intruded the more primitive gabbros at a later stage. Composition of the studied samples varies considerably from sample to sample, between clinopyroxene and plagioclase-rich gabbros, but the content of oxides (mostly magnetite and ilmenite) is between 5-10%. The studied sample have well-developed foliation, but lineation is not well marked. In general, plagioclase occurs as equigranular aggregates, whereas clinopyroxene occurs predominantly as porphyroclasts. Olivine occurs as equigranular, idiomorphic grains within the gabbros, but also as "pods" rich in olivine in pressure shadows of clinopyroxenes. Ilmenite and magnetite occur along bands parallel or oblique to the foliation.

METHODS

The crystallographic preferred orientations of the studied samples were determined by electron backscatter diffraction technique (EBSD) in a scanning electron microscope. All the samples were measured in a FEI Quanta 200F with EDAX Hikari EBSD camera operating at the Scientific Centre for Optical and Electron Microscopy (ScopeM) of ETH Zürich. All the samples were mechanically polished to a 0.25 µm diamond suspension and chemically-mechanically polished with an alkaline solution of colloidal silica (0.025 µm) for 3-10 minutes on a neoprene polishing cloth. All the EBSD maps were acquired using an accelerating voltage of 20 kV, beam current of 8 nA, working distance of 17 mm, and variable stepsizes, from 0.5 to 1 µm, depending on the scale of the map. With the exception of the olivine-antigorite sample, all the EBSD maps used 4 x 4 binning of the patterns. The antigorite was indexed using the structure determination of Capitani and Mellini (2006), using an a-axis of 35 Å, typical of high-temperature antigorite. As antigorite

generates poor patterns in the above standard EBSD mapping conditions, a binning of 2 x 2 combined with a pixel Hough binning of 160 and about 120 reflectors were used for the correct indexation. Post-acquisition processing in the EDAX-OIM 8 software included the standardization of the confidence index (CI) using a minimum grain tolerance angle of 10°, and minimum 10 indexed pixels per grain, followed by a CI correlation between neighbor points, where pixels with low CI (<0.1) are reassigned to the orientation and the CI of the neighbor data point with highest CI in the individual grains. All the EBSD maps and calculations and plots were carried out with the MTEX toolbox for MATLAB (Hielscher and Schaeben, 2008). The orientation distribution functions (ODFs) were calculated using the complete datasets with the de La Vallee Poussin kernel with a half-width of 10°, which is equivalent of a bandwidth of 28 in the spherical harmonic coefficients. All the data is plotted in equal-area, upper hemisphere pole figures, with a resolution of 5°. Interphase misorientation pairs between phase A and phase B were calculated for the entire maps using a common misorientation threshold of 10°, and therefore low angle interphase misorientations, if present, are not studied here. Detected grains with less than 10 pixels were also not considered in the calculations.

RESULTS

Calcite – Aragonite

In the studied sample, calcite is the dominant phase (~75% sample) while aragonite is secondary (making up the other ~25% - Fig. 2a). Calcite grain size varies between 25 µm -120 µm, some of the large grains are heavily twinned, and most of the large calcite grains have large internal misorientations, up to angles of 10° (Fig. 2b). The aragonite occurs predominantly wrapped around the calcite large grains along discontinuous, anastomosing bands (Fig. 2a, c), except for the small aggregate of coarser grain aragonite that occurs in the bottom of the Fig. 2a. It has grain sizes varying from 4 µm to 12 µm, and from the orientation maps, it seems that the crystallographic preferred orientation of both calcite and aragonite is

very weak (Fig. 2a, d). This is confirmed on the pole figures (Fig. 3), where both minerals show a weak CPO, with calcite being slightly stronger than aragonite (4.3 multiples of uniform distribution of calcite against 2.6 from aragonite). The pole figures are also used here to look for possible similarities between different poles of the studied mineral pairs, which may indicate that the development of a CPO of phase 2 is crystallographically controlled by phase 1, but do not fully proof that both phases have any orientation relationship along the interfaces . A careful comparison between the pole figures of both phases shows similarities. For instance, the [100] axes of aragonite are distributed in a broad girdle that is parallel to a similar girdle of poles to (2 $\bar{1}$ $\bar{1}$ 0) of calcite, whereas the distribution of [001] of aragonite is similar to the distribution of (0 1 $\bar{1}$ 8) of calcite. In addition, the strongest concentration of [010] and [110] in aragonite are subparallel to the maximum concentrations of (0001) and (1 0 $\bar{1}$ 4) of calcite, respectively.

The uniform misorientation angle distribution (i.e. the misorientation distribution expected in the case of a uniform, "random" ODF) shows a progressive increase in frequency to a maximum of 90° (Fig. 4a) and a sudden drop to a maximum misorientation angle ~92° (for the trigonal-orthorhombic relationship). The uniform misorientation axis distribution (Fig. 4b) has a weak maximum parallel to the poles of ($\bar{6}$ 2 4 5) and symmetrically related, which are about 10° from the poles to (1 $\bar{2}$ 1 0), with a maximum of uniform distribution (MUD) around 2.5. The misorientation angle distribution for correlated (neighbor) interphase boundaries tend to follow the distribution expected in the case of a uniform distribution (Fig. 4c). In detail however, the red bars that represent the misorientation angle between neighbor phase boundaries show that the peaks between 25° to 50° occur in higher frequencies than the ones expected in the case of non-neighbor pairs (red line) or uniform distribution (orange line). This suggests that phase boundaries within this angle range show some sort of physical relationship that the uncorrelated distribution does not present, which might indicate a special orientation relationship between calcite and aragonite.

For the orientation relationship (11-20)calcite || (100)aragonite and [0001]calcite || [110] aragonite, the misorientation axis is 54.2°, and the misorientation axis is parallel to (2 $\bar{1}$ $\bar{1}$ 0) in the calcite reference

frame and to (100) in the aragonite reference frame. If we now plot the misorientation axes for the whole range of misorientation angles for the calcite-aragonite phase boundaries, there is a vast distribution around the primitive circle of the steronet and a weak maximum parallel to the pole of (2 $\bar{1}$ $\bar{1}$ 0), in agreement with a dominant topotactic relationship transformation between calcite and aragonite (Fig. 4d). Note that due to the symmetry, only two out of four symmetrically equivalent pole to planes of aragonite are parallel to two out of three pole to planes in calcite, which are $(1\ \bar{1}\ 0\ 8)_{cal}$ || $(\ \bar{1}\ 1\ \bar{3})_{ar}$ and $(\ \bar{1}\ 0\ 1\ \bar{8})_{cal}$ || $(\ \bar{1}\ \bar{1}\ 3)_{ar}$. The interface trace map in the Figure 4e shows a broad range of distribution of misorientation angles for the interface traces, but about 41% of the phase boundaries between calcite and aragonite have a range of misorientations between 40-70°.

Olivine – Antigorite

The sample MR-1 contains about 60% of hydrous phases (chlorite, tremolite and antigorite), and about 40% of the lithospheric mantle olivine framework is still preserved (e.g. Fig. 5a), and its microstructure is detailed described in Morales et al. (2013). The thin section studied here was cut normal to the antigorite foliation and parallel to the dominant lineation. The phase boundaries between olivine and the hydrous phases in this sample are predominantly straight and sharp, while the contacts between hydrous phases might be blurred and difficult to identify visually.

Olivine and antigorite bulk crystallographic preferred orientation is given in the Figure 6. Due to the relatively coarse grains and the dismembering due to the antigorite, the olivine CPO is relatively complex but not very strong (maxima of 3.9 MUD), with [100] orientated around 20° from the antigorite lineation and [010] and [001] distributed along incomplete girdles, normal and parallel to the XZ plane respectively.. Antigorite on the other hand has a strong texture (8.5 MUD for (001) and has a typical (001) fiber-texture, with the poles of (001) strongly orientated at a small angle to the pole of the foliation and the poles of (100) and (010) distributed along girdles parallel to the reference foliation. Although it is not

possible to establish clear orientation relationships between olivine and antigorite primary maxima from these figures, in detail the secondary maxima show some similarities. For instance, the secondary maxima of olivine [010] and [001] close to Z is parallel to the maxima of poles to (010) of antigorite.

The uniform misorientation angle distribution for olivine-antigorite (Fig. 7a) shows a progressive increase up to a maximum peak at 90°, when it drops down substantially, reaching a maximum misorientation angle ~120° for the combination of orthorhombic-monoclinic. The uniform misorientation axis distribution (Fig. 7b) shows a maximum peak on <947>, with a MUD 1.6. The correlated misorientation angle distribution shows some peaks that are much higher than the expected distribution of non-correlated phase boundaries or the misorientation expected in the case of uniform ODF. In particular, the misorientation angles between 70°-100° are considerably higher. If the misorientation angle is now limited to this angular range, the resulting misorientation axis plot show a maximum parallel to the poles (094), which lies about 30° from [010]. This is almost equivalent to the [5 $\bar{9}$ 4] axis described in Morales et al. (2018). The interphase boundary map presented in the Figure 7e shows that about 48% of the interfaces between olivine and antigorite have a range of misorientations between 80-100°, from which 27% have a 10° misorientation range of 90-100°.

Magnetite – hematite

In the studied sample, magnetite comprises ~60% and hematite ~40% and present a massive structure. Hematite nevertheless seem to occur in “patches” on the EBSD map (Fig. 8a). Magnetite shows almost an uniform distribution of its main crystal directions [100], [110] and [111], with only [100] showing some degree of orientation subparallel to Z in the sample reference frame (Fig. 9a). Hematite CPO on the other hand is better developed (Fig. 9b) and shows a maximum concentration of poles to (0001) parallel to Y and a more complex distribution of poles of (1 0 $\bar{1}$ 0) and (1 0 $\bar{1}$ 1). At first it seems that is no clear relationships between the pole figures of magnetite and hematite. However, as magnetite is cubic, a

rotation of 90° around x in the pole figure is allowed and would bring this maximum into parallelism with hematite (0001) pole figure.

The uniform misorientation angle distribution of magnetite-hematite shows a peak around 42° (Fig. 10 a), followed by a fast drop to the maximum possible interphase misorientation angle between these two phases, around 60°. The uniform misorientation axis distribution (Fig. 10b) shows a maximum peak on <231>, with a MUD 3.5. The interphase misorientation angle distribution for neighbor crystals follows the same trend for the uncorrelated grains, or the distribution expected in the case of uniform distribution (Fig. 10c). Nevertheless, it shows frequencies around 5% higher than the frequency expected in the case of uniform distribution. The correlated interphase misorientation axis (Fig. 10d) show a similar distribution as the uniform one, but only one stronger concentration parallel to [231] with MUD of ~8, with the other symmetrically equivalents ([$\bar{3}$ 2 1], [$\bar{2}$ $\bar{3}$ 1],[3 $\bar{2}$ 1]) showing weaker concentrations. The interphase boundary map (Fig. 10e) shows that 73% of the interphase boundaries have misorientations between 30-50°, and 41% lie in a range of 40-50°.

Plagioclase – Olivine – Ilmenite

In the studied sample of gabbro from the Atlantis bank, plagioclase is the dominant phase, and together with clinopyroxene, are the primary phases to crystallize in this sample. Plagioclase are predominantly subhedral, grain size varies from 100 to 600 µm (Fig. 11a) and a considerable number of grains still preserve magmatic twinning. The smaller plagioclase grains are interpreted as plagioclase subgrain rotation recrystallization (Allard et al., 2021Plagioclase CPO is relatively weak, as seen in the orientation map with a large variety of colors (Fig. 11c). Olivine on the other hand occurs predominantly as anhedral grains that are much smaller in grain sizes (50-100 µm). In this sample, olivine seems to be (at least in part) a late phase, as it commonly occurs along interstitial spaces between plagioclase and diopside grain/phase boundaries, and along pressure shadows in clinopyroxene porphyroclasts. Ilmenite grains are

mostly anhedral in shape, grain sizes are between 20-70 μm, and occur predominantly in contact with plagioclase (Fig. 11a).

The pole figures for plagioclase, olivine and ilmenite are plotted in a sample reference frame where the foliation is vertical N-S (so the pole of the foliation is at E in the pole figure), and the lineation also N-S, but horizontal (Fig. 12). All the pole figures show a weak crystallographic preferred orientation. Plagioclase (100) poles are distributed along a broad, asymmetrical girdle cross-cutting Y, while the poles to the (010) are mainly concentrated at an angle of ~15° with the pole of foliation. Olivine [100] axes are predominantly concentrated parallel to Y, [010] and [001] broadly distributed with weak maxima parallel to the pole of the foliation (the former) and parallel to the lineation (the later). The poles to the (0001) of ilmenite are preferentially aligned with Y, while the poles to the (1 0 $\bar{1}$ 1) rhombs are at low angle with the pole of the foliation Z and the poles to the (1 0 $\bar{1}$ 0) prisms subparallel to the lineation, but showing secondary, symmetrically related maxima every ~60°. More important than the CPO strength in this case though are similarities in the pole figures. For instance, the distribution of [100] and [010] of olivine shows similarities with the poles to the (100) and (010) of plagioclase, while the poles to the (0001) and (10-10) of ilmenite shows similarities with the poles to the (100) of plagioclase, and the distribution of poles to the (10-11) ilmenite are comparable to the poles to the (010) planes of plagioclase (Fig. 12).

The misorientation angle distribution assuming a uniform distribution show, for the plagioclase-olivine, a peak at misorientation angles ~83° and a sudden drop to a maximum misorientation of ~119° (Fig. 13a). Due to the triclinic-orthorhombic combined symmetry (plagioclase-olivine), the misorientation axes have to be presented in both upper and lower hemisphere, where the maximum misorientation angle expected in the case of a uniform distribution is subparallel to the <253> of olivine, with a MUD of 1.7 (Fig. 13b). In the case of plagioclase-ilmenite, the maximum misorientation angle expected in the uniform case is ~90°, with frequencies dropping progressively to a maximum angle of 180° (Fig. 13c). The maximum misorientation angle in the combination of plagioclase-ilmenite symmetries seems to be distributed all

over along the primitive circle of the stereonet, and only statistical calculations allows to pinpoint a maximum parallel to the poles to the {3 2 $\bar{1}$ 0} planes of ilmenite and subparallel to [100] of plagioclase, with a MUD of 3 (Fig. 13d).

The distribution of interphase misorientation angles for neighbor (correlated) plagioclase-olivine grains show abnormal frequencies for misorientation angles between 65 and 90° (>2% of the uncorrelated/uniform distribution – Fig. 14a). If we limit the range of misorientation angles to the one above and plot the misorientation axes, the orientation is not very strong (2.5 MUD), but it shows a maxima parallel to the pole to the (100) of plagioclase, 2 other maxima with similar MUD, and a secondary maxima parallel to [010] of plagioclase (parallel to the pole to the (010) plane – Fig. 14b). The misorientation angle distribution for the pair plagioclase-ilmenite shows a variety of higher frequency peaks intercalated with lower frequency peaks (Fig. 14c), when compared with the uncorrelated/uniform distributions. Also, the studied sample does not show misorientation peaks larger than 165°. For simplicity, we focus on the misorientation peaks between 85-130°. When limited to this range, most of the misorientation axes are parallel to the [100] of plagioclase, with a MUD of 9. The interphase boundary map (Fig. 15a) shows that about 70% of the boundaries between plagioclase and olivine have a narrow range of misorientations between 60 and 100°, while in the case of plagioclase-ilmenite the range is more variable (Fig. 15b), and about 50% of the interphase boundaries between these two phases have a range of misorientations between 60 and 120°.

IMPLICATIONS

Easier assessment of interphase boundary orientation relationships

Differently from grain boundaries separating grains of same composition and structure, interphase boundaries are interfaces that normally separate grains with different structures and / or compositions.

Because of this complexity, only individual interfaces are normally studied at the time, in most cases via selected area diffraction (SAD) in a transmission electron microscope (TEM). SAD-TEM provides very detailed information in terms of angular and spatial resolution of orientation relationships between the two phases separated by the interface (atomic scale resolution with angular resolutions <0.1 °) at the expenses of statistical representation. Electron-transparent sample preparation for TEM is not trivial and for certain geological materials can be challenging. As an example, to prepare standard in-situ TEM lamellae via focused ion beam techniques, one needs around two hours. However, one has to consider that the dimension of such a sample is around 15x10 µm (length x deep), and ~100 nm thick, so in the case of a very fine-grained material, one may observe a few interphase boundaries, but in the case of a more coarse-grained rock, one might be able to see only one interface. In addition, TEM operation and correct indexation of diffraction patters from SAD (particularly for low-symmetry phases) is more complex and time consuming than SEM operation and EBSD mapping and require extensive training to be done effectively. As demonstrated here with EBSD maps, one can see a statistically representative number of interfaces on samples that have different phases and different grain sizes. As we know the orientation of the grains separated by the interface, we can then calculate the misorientation angle/axis between these two grains, which can be used to infer possible orientation relationships between the two phases. As an example, we know that $(11\text{-}20)_{cal} \parallel (100)_{ara}$ and $[0001]_{cal} \parallel [011]_{ara}$. If we know now the orientation of the daughter phase (in this case, aragonite), we can compute the orientation of the parent phase following the MTEX script presented in the supplementary material.

The intention here is not to say that EBSD-derived interphase misorientation is a substitute for TEM analysis. If fact, the idea is to use EBSD mapping to precisely locate the orientation and misorientation of specific interphase boundaries and use this data to select the interfaces one wants to study in more detail in the TEM. The interphase misorientation analysis does not give us the degree of coherency between the phases separated by the interface, nor any atomic resolution along the interface separating two minerals. On the other hand, once you have an EBSD map, you can test possible misorientation relationships

between any phase present in the map. That was the case of the gabbro sample whose results are presented in the Figs. 11-15, we have tested all the possible pairs of phases within the map and found that plagioclase-olivine and plagioclase-ilmenite have an orientation relationship that can further be analyzed in the TEM.

Interphase orientation relationships

Phase transformations in geological materials leading to interphase orientation relationships between parent→daughter phases occur predominantly by two major mechanisms: martensitic and nucleation/growth mechanisms. From the four different systems studied in this paper, two belong to the nucleation/growth mechanism (olivine→antigorite and magnetite→hematite), one can be either interpreted as a martensitic or nucleation/growth (calcite→aragonite), and are discussed in a bit more detailed below. In fact, martensitic transformations have been referred in the material sciences literature as a type of nucleation/growth type of transformation that occurs in much shorter time scales (e.g. Olson and Morris-Cohen, 1972; Guimarães and Rios, 2008). Plagioclase→olivine and plagioclase→ilmenite on the other hand do not represent phase transformation of any sort, but because the misorientation angle/axis pair show what looks like special relationships, these results are discussed in terms of orientated growth below.

Nucleation and growth mechanisms are normally associated with diffusion and therefore tend to be thermally activated or enhanced. The growth of one phase into another also depends on the interfacial free energy, the Gibbs free energy of the reaction and the strain free energy (e.g. Mainprice et al., 1990, Porter and Easterling, 1992). Phase transformation from parent phase to daughter phase may occur by only changing the structure from the parent phase (e.g. calcite-aragonite) or by changing both the composition structure between the two phases (e.g. magnetite-hematite or olivine-antigorite). This process starts with the homogenous (or heterogeneous) nucleation of the daughter phase. The homogeneous nucleation is

controlled by the energy to form the nucleus of the daughter phase, and because of that, it requires activation energies much higher than those required for heterogeneous nucleation (e.g. Porter and Easterling, 1992; Sunagawa 1994). Heterogeneous nucleation refers to the nucleation of the daughter phase along the parent phase substrate and requires much less activation energy because the interface between the old and new phases reduces considerably the surface energy value. Heterogeneous nucleation normally occurs along intracrystalline defects (dislocations, grain/interphase boundaries) or due to the presence of inclusions, where the initial nuclei of the daughter phases growth normally by diffusion processes.

Classical examples of this mechanism include the hydration of olivine and formation of antigorite and the transformation of magnetite into hematite. Plümper et al. (2012) showed that the initial exchange of Fe-Mg along (100) dislocation walls in olivine lead to the first steps of topotactic formation of antigorite along this plane in olivine, something also observed in Boudier et al. 2010. As demonstrated in the Fig. 7c, the higher frequency interphase misorientation angle are between 80-100°, with a dominant misorientation axis parallel to the poles to the (094), which departs 15° from the interphase misorientation axes parallel to the poles to the (5-94) determined in Morales et al. (2018). Considering that the sample studied here is less deformed and has the olivine grain network much better preserved than the antigorite schist studied in the aforementioned study, we conclude that the interphase misorientation relationships are compatible with the type 4 phase transformation of $(010)_{ol} \parallel (210)_{atg}$ and $[100]_{ol} \parallel [001]_{atg}$, determined by Morales et al. (2018) using the interphase misorientation angle/axes.

Calcite-aragonite transition and the orientation relationships between the two phases has been extensively studied in the past (e.g. Carlson and Rosenfeld, 1981; McTigue and Wenk, 1985; Gillet et al., 1987) and two main mechanisms for the phase transformation has been proposed. While the experimental results suggest that the heterogeneous nucleation and topotactic growth is the dominant mechanism under a variety of conditions, in agreement with the model from Carlson and Rosenfeld (1981), Gillet and Madon

(1982) proposed a martensitic mechanism for the calcite-aragonite transition. In this model, stacking faults dragging by partial dislocation movement is responsible for the phase transformation. In contrast to (normally) slow nucleation and growth mechanisms, martensitic phase transition can be a very fast mechanism, normally producing a metastable phase. Martensitic transformation occurs by the progressive and systematic shearing of the lattice of the parent phase in a way that the distance in which any atom moves is less than one atomic spacing, which implies that the lattice is distorted, but the atoms retain the same neighbors. Because of that, martensitic transformation only leads to change in the structure of the phases, and not in composition, in order to accommodate the shearing described above.

Gillet et al. (1987) described the dominant phase transition orientation relationship for calcite→aragonite as $(11\bar{2}0)_{cal}$ || $(100)_{ara}$ and $[0001]_{cal}$ || $[011]_{ara}$. McTigue and Wenk (1985) on the other hand described $(11\bar{2}0)_{cal}$ || $(010)_{ara}$, $(10\bar{1}4)_{cal}$ || $(011)_{ara}$ and $[r2:f1]_{cal}$ || $[001]_{ara}$. The predominant misorientation angle of 54.2° with a dominant axis parallel $(2\bar{1}\bar{1}0)$ of calcite reference frame of the studied sample indicate that in general, the transformation orientation relationship in this case is the one described by Gillet et al. (1987). However, when the misorientation angle is limited to a narrow range between 25° and 50°, the misorientation axis change to parallel to the pole to the $(01\bar{1}8)$ which is the twin plane of e-twins in calcite. Although we don't have access to the orientation of the interface along twin planes, it seems from the EBSD map that the red interphase boundary traces are visually subparallel to the twin planes, for example, of the grains on top-left of the map (Fig. 4e). This observation is in agreement with the Fig. 2a-b, where a number of aragonite grains occur wrapped around a heavily twinned calcite grain, and those grains in contact with that specific calcite grain are the ones that produce the misorientation axis subparallel to $(01\bar{1}8)$.

Transformation from magnetite to hematite is another example of nucleation and growth mechanism, where hematite growths topotactically on magnetite, following the main orientation relationship $(111)_{mag}$ || $(001)_{hem}$ and $(-101)_{mag}$ ||$(100)_{hem}$ (Heizmann et al., 1981, Lagoeiro, 1998, Barbosa and Lagoeiro, 2010).

These authors described other orientation relationships, and the transformation magnetite-hematite-magnetite is, in their case, reversible and always topotactically controlled. The misorientation angle for the topotactic orientation described above is ~56°, and the misorientation axis is parallel to <793> of magnetite, which is about 4° from the direction <231> expected in the case of a uniform distribution (Fig. 10b) As we see in the histogram from Figure 10c, all the misorientation angles above 40° occur in higher frequencies than the frequencies expected in the case of a uniform distribution, with the highest bin showing misorientations between 45-50°. However, the misorientation axis is very close to the one expected in the case of a random orientation of both magnetite and hematite. As demonstrated in the pole figures (Fig. 9), hematite CPO is stronger than magnetite, and no clear relationship between the pole figures can be made, unless we consider a rotation of 90° of magnetite around x, which would bring the maximum now at the S to parallelism with (0001) hematite. That would imply however that, in this specific sample, we have a $(100)_{mag} \parallel (001)_{hem}$ sort of relationship. Although this may represent a new possible topotactic orientation relationship, one must consider that the studied EBSD map has a very large number of grains and already around 40% of hematite. At these conditions, it is difficult to imagine that every single crystal of hematite resulted from the transformation of magnetite on one of the symmetrically related $(111)_{mag}$ planes. I believe that the transformation magnetite-hematite is indeed initiated along $(111)_{mag}$ as clearly shown by Barbosa and Lagoeiro (2010), but once the reaction "kicks in", hematite started to be dissolved along other low index interfaces, and the initial orientation relationship is progressively lost. Deformation localization in iron ores like the studied sample normally leads to the oxidation of magnetite and consequent transformation to hematite, and deformation is predominantly accommodated by hematite. In this case, hematite can develop stronger CPOs than magnetite (e.g. Morales et al., 2008) and that may potentially affect the interphase misorientation distribution angles. It seems that in all studied cases here, transformation from parent to daughter phase occurs preferentially (but certainly not exclusively) following certain orientation relationships.

Exploring unknown orientation relationships

So far, we have explored the interphase misorientation analysis in examples where we know that the orientation of a daughter phase is partially/completely controlled by the orientation of the parent phase. However, if one has EBSD orientation maps of "normal" rocks (polymineralic), one can explore potential interphase misorientation angle/axis relationships and find possible "orientation relationships" between the phases presented in this map Naturally we shall not expect that all the phases will have any sort of relationship with the other phases in the aggregate, but let's take the example of the oxide-rich gabbro studied here. The EBSD map of this sample has 6 different minerals (plagioclase, clinopyroxene, olivine, pargasite, ilmenite and magnetite – Fig. 11 only shows the three where orientation relationships were found). Tests conducted in all possible pairs of minerals within this list resulted in 15 different interphase misorientation angle/axis pairs. From these 15 pairs, only 2 (plagioclase-olivine and plagioclase-ilmenite) have shown some sort of orientation relationships between the two phases. In both cases, the orientation relationships have nothing to do with nucleation/growth nor martensitic transformations, as the minerals have different compositions and structures. The orientation relationships between plagioclase-olivine and plagioclase-ilmenite seem in the studied sample seem to be related to some sort of epitaxial growth of olivine and ilmenite on plagioclase, possibly controlled by the surface energy of plagioclase and wetting surfaces on this phase.

In the studied sample, plagioclase (together with diopside) are the primary phases and crystallize first in their magmatic history, while both olivine and (later) ilmenite seem to be residual melts that crystallized later in the gabbro history. The surface energy along a solid-liquid interface is mainly controlled by the atomic structure on the interface, which in turn is dependent to its crystal orientation (e.g. Laporte and Watson, 1995). In addition, the crystallization of second phases using a host crystal as "substrate" depends on the crystal structure between the two phases, and any possible relation orientation between the host and the precipitate depends on the fit of lattice space between these two phases (e.g. Sutton and Balluffi,

1994). In the case of the studied gabbros, the interphase misorientation axis for the pair plagioclase-ilmenite is subparallel to plagioclase [100]. If we assume that the interphase misorientation axis is contained along the interface, in a similar fashion as tilt grain boundaries (e.g. Lloyd. 2004), and if we assume that the interface has a high tilt angle, this interface of plagioclase can anything between (010) or (001). Although this is the topic of another publication in preparation, we know the distance between the oxygen atoms connecting the SiO4 – AlO4 tetrahedra in labradorite is between 4.23 and 4.26 Å , based on the determinations of Wenk et al (1980). This distance is very close to the distance between O-Fe-O along the long axis of FeO_6 octahedra of ilmenite, which is 4.224Å, determined by Wechsler and Prewitt (1984) and visualized with CrystalMaker ®. Although plagioclase is either monoclinic or triclinic and ilmenite is trigonal, is it not uncommon to find higher symmetry in certain plagioclase crystal direction. For example, plagioclase is surprisingly symmetrical along [001] as noticed by Wenk et al. (2011) and Ageeva et al. (2020), Along this direction, there are six-component tetrahedra "rings" that can easily accommodate the FeO_6 octahedra from ilmenite. If ilmenite is then the late phase, it can crystallize using the pre-existent plagioclase as substrate, where the FeO_6 octahedra is e accommodated along plagioclase [001] axis by sharing some of the oxygen atoms in the crystalline structure of plagioclase (substrate) with those with similar distances (precipitate). Although more detail is needed and it is out of scopus of this paper, it is possible that ilmenite (0001) plane and [1 0 $\bar{1}$ 0] direction of ilmenite are parallel to (120)/ ($\bar{1}$ 20) planes and [001] direction of plagioclase, respectively, previously reported in Wenk et al., (2011), or to one of the parallelism relationships described in Ageeva et al., (2016).

As a final remark, the calculation of interphase misorientations from EBSD maps is a potential tool to, for example (i) study topotactic relationships between minerals, (ii) explore potential "orientation relationships" of different phases in a rock, (iii) to plot interphase boundaries with variable misorientation in a map, and highlight those which have special misorientation angles/axis and even possible orientation relationships and (iv) to use those maps to precisely pinpoint specific interfaces that can be further analysed with TEM, using target preparation with focused ion beam methods for example. Steps for the

calculations include (i) calculate the interphase misorientation angle distribution assuming uniform ODFs for both phases, (ii) calculate the actual correlated and uncorrelated misorientation angle distribution for the two studied phases, (iii) compare the correlated misorientation with the uncorrelated/uniform distributions in a histogram and find correlated misorientation peaks that are more frequent than those calculated for a uniform/uncorrelated distribution. After that, one can (iv) limit the misorientation angle to those higher frequent peaks of any range and then plot those in inverse pole figures of combined crystal symmetries and (v) plot the different range of interphase misorientations directly on EBSD maps. If for example topotactic relationships exist between the two phases, one can calculate what is the pair misorientation angle/pair for such a relation, and look into an EBSD map for the presence of these relationships, based on a misorientation angle range that includes the specific misorientation angle for the specific topotactic relationship.

ACKNOWLEDGEMENTS

I would like to thanks Sebastian Cionoiu and Lucie Tajcmanova for the calcite-aragonite sample, and Jessica Till for the gabbro sample. I am also grateful for the detailed reviews by Luca Menegon and the anonymous reviewer, which improved considerably the quality of the paper, and by the editorial handling of Dr. Sergio Speziale.

REFERENCES CITED

Ageeva O, Habler G, Topa D, Waitz T, Li C, Pertsev A, Zhilicheva O, Abart R (2016) Plagioclase hosted Fe-Ti-oxide micro-inclusions in an oceanic gabbro-plagiogranite association from the Mid Atlantic Ridge at 13° 34’ N. American Journal of Science 316:85–109

675 Ageeva, O., Bian, G., Habler, G., Pertsev, A., Abart, R. (2020). Crystallographic and shape orientations
676 of magnetite micro-inclusions in plagioclase, Contributions to Mineralogy and Petrology 175: 95, 020)
677 175:95, doi.org/10.1007/s00410-020-01735-8.
678
679 Alkmim, F., Marshak, S., (1998) Transamazonian orogeny in the southern São Francisco craton region,
680 Minas Gerais, Brazil: evidence for Paleoproterozoic collision and collapse in the Quadrilátero Ferrífero.
681 Precambrian Research 90, 29–58.
682
683 Barbosa, P. F., Lagoeiro, L.E. (2010). Crystallographic texture of the magnetite-hematite transformation:
684 Evidence for topotactic relationships in natural samples from Quadrilátero Ferrífero, Brazil. American
685 Mineralogist 95, 118-125.
686
687 Bestmann, M.; Prior, D.J. (2003). Intragranular dynamic recrystallization in naturally deformed calcite
688 marble: diffusion accommodated grain boundary sliding as a result of subgrain rotation recrystallization.
689 Journal of Structural Geology 25, 1597-1613
690
691 Boudier, F., Baronnet, A., Mainprice, D. (2010). Serpentine mineral replacements of natural olivine and
692 their seismic implications: oceanic lizardite versus subduction-related antigorite. Journal of Petrology 51
693 (1–2), 495–512, http://dx.doi.org/10.1093/petrology/egp049.
694
695 Carlson, W.D., Rosenfeld, J.L. (1981) Optical determination of topotactic aragonite-calcite growth
696 kinetics: metamorphic implications. Journal of Geology 89, 615-638
697
698 Cionoiu, S. (2019). Experimental and Numerical Predictions of Phase Transitions in Solids under
699 Differential Stress. PhD Thesis, ETH Zürich. https://doi.org/10.3929/ethz-b-000353445
700

701 Duyster, J., Stöckhert, B. (2001) Grain boundary energies in olivine derived from natural microstructures.
702 Contributions to Mineralogy and Petrology 140 (5), 567-576.
703
704 Faul, U.H., Fitz-Gerald, J. (1999) Grain misorientations in partially molten olivine aggregates: an electron
705 backscatter diffraction study. Contributions to Mineralogy and Petrology 26, 187-197
706
707 Gillet, P., Gerard, Y., Williame, C. (1987) The calcite-aragonite transition: mechanism and microstructure
708 induced by transformation stresses and strain. Bulletin de Minéralogie 110, 481-496.
709
710 Guillet, P., Madon, M., (1982) Un modèle de dislocations pour la transition aragonite-calcite. Bulletin de
711 Minéralogie 105, 590-597.
712
713 Hielscher, R., Schaeben, H. (2008) A novel pole figure inversion method: specification of the MTEX
714 algorithm. Journal of Applied Crystallography 41, 1024–1037. http://
715 dx.doi.org/10.1107/S0021889808030112.
716
717 Hiraga, T., Anderson, I. M., Kohlstedt, D. L. (2004) Grain boundaries as reservoirs of incompatible
718 elements in the Earth's mantle. Nature 427, 699-703
719
720 Hunter, W.C., Smith, D. (1981) Garnet peridotite from Colorado Plateau ultramafic diatremes: hydrates,
721 carbonates and comparative geothermometry. Contributions to Mineralogy and Petrology 76, 312–320.
722
723 Karson, J. A., Lawrence, R. M. (1997) Tectonic window into gabbroic rocks of the middle oceanic crust in
724 the MARK area near Sites 921–924, Proceeding of the Ocean Drilling Program Scientific Results, 153,
725 61–76, doi:10.2973/odp.proc.sr.153.005.1997.
726

Kelemen, P. B., Kikawa, E., Miller, D. J. and the Shipboard Scientific Party (2007), Leg 209 summary: Processes in a 20- km-thick conductive boundary layer beneath the Mid-Atlantic Ridge, 14_–16_N, Proc. Ocean Drill. Program Sci. Results, 209, 1–33, doi:10.2973/odp.proc.sr.209.001.2007.

Kilian, R., Heilbronner, R., and Stunitz, H. (2011). Quartz grain size reduction in a granitoid rock and the transition from dislocation to diffusion creep. Journal of Structural Geology 33, 1265–1284, https://doi.org/10.1016/j.jsg.2011.05.004

Krakow, R., Bennet, R.B., Johnstone, D.N., Vukmanovic, Z., Solano-Alvares, W., Laine, S.J.,Einsle, J.F., Midgley, P., Rae, C., Hielscher, R. (2017) On three-dimensional misorientation spaces. Proceedings of the Royal Society A 473: 20170274. http://dx.doi.org/10.1098/rspa.2017.0274

Kruhl, J., Wirth, R., Morales, L.F.G. (2013) Quartz grain boundaries as fluid pathways in metamorphic rocks. Journal of Geophysical Research Vol. 118(5), 1957–1967. doi:10.1029/2012JB009644

Lagoeiro, L.E. 1998. Transformation of magnetite to hematite and its influence on the dissolution of iron oxide minerals. Journal of Metamorphic Petrology 16, 415-423

Laporte, D., Watson, E. B. (1995) Experimental and theoretical constraints on melt distribution in crustal sources: The effect of crystalline anisotropy on melt interconnectivity, Chemical Geology 124, 161–184, doi:10.1016/0009-2541(95)00052-N.

Lloyd G.E., Farmer A.B., Mainprice, D. (1997) Misorientation analysis and the formation and orientation of subgrain and grain boundaries. Tectonophysics 279, 55-78.

Lloyd, G. E. (2004) Microstructural evolution in a mylonitic quartz simple shear zone: the significant roles of dauphine twinning and misorientation. In: Alsop, G. I., Holdsworth, R. E., McCaffrey, K. &

Handy, M. (eds) Transports and Flow Processes in Shear Zones. Geological Society, London, Special Publications, 224, 39–61.

Mainprice, D., Humbert, M., Wagner, F. 1990. Phase transformations and inherited lattice preferred orientations: implications for seismic properties. Tectonophysics 180, 213-218.

Mainprice, D., Lloyd, G.E., Casey, M. (1993) Individual orientation measurements in quartz polycrystals - advantages and limitations for texture and petrophysical property determinations. Journal of Structural Geology 15, 1169-1187

Marquardt, K., Rohrer, G.S., Morales, L., Rybacki, E., Marquardt, H.; Lin, B. (2015). The most frequent interfaces in olivine aggregates: The GBCD and its importance for grain boundary related processes. Contributions to Mineralogy and Petrology 170:40, doi: 10.1007/s00410-015-1193-9.

Marti, S., Stünitz, H., Heilbronner, R., Plümper, O., Kilian, R. (2018) Syn-kinematic hydration reactions, grain size reduction, and dissolution–precipitation creep in experimentally deformed plagioclase–pyroxene mixtures. Solid Earth, 9, 985–1009 https://doi.org/10.5194/se-9-985-2018

McGetchin, T.R., Silver, L.T. (1970) Compositional relations in minerals from kimberliticand related rocks in the Moses Rock Dike, San Juan County, Utah. American Mineralogist 55, 1738–1771.

McLaren, A. C. (1986) Some speculations on the nature of high angle grain boundaries in quartz rocks, in Mineral and Rock Deformation: Laboratory Studies: The Paterson Volume, pp. 233–245, AGU, Washington, D. C.

McNamara, D. D., Wheeler, J., Pearce, M., & Prior, D. J. (2012). Fabrics produced mimetically during static metamorphism in retrogressed eclogites from the Zermatt-Saas zone, Western Italian Alps. Journal of Structural Geology 44, 167-178. http://dx.doi.org/10.1016/j.jsg.2012.08.006

McTigue Jr., J.W., Wenk, H.-R. (1985) Microstructure and orientation relationshiops in the dry-state aragonite-calcite and calcite-lime phase transformations. American Mineralogist 70, 1253-1261

Menegon, L., Nasipuri, P., Stünitz, H., Behrens, H., Ravna, E. (2011). Dry and strong quartz during deformation of the lower crust in the presence of melt. Journal of Geophysical Research 116, B10410. http://dx.doi.org/10.1029/2011JB008371.

Menegon, L., Piazolo, S., Pennacchioni, G. (2010). The effect of Dauphiné twinning on plastic strain in quartz. Contributions to Mineralogy and Petrology. 161, 635–652.

Miranda, E.A., John, B.E. (2010) Strain localization along the Atlantis Bank oceanic detachment fault system, Southwest Indian Ridge. Geochemistry, Geophysics, Geosystems 11(4), doi:10.1029/2009GC002646

Morales, L.F.G., Mainprice, D., Boudier, F. (2013) The influence of hydrous phase on the microstructure and seismic properties of a hydrated mantle rock. Tectonophysics 594, 103–117.

Morales, L.F.G., Mainprice, D., Kern, H. (2018) Olivine-antigorite orientation relationships: microstructures, phase boundary misorientation and seismic properties. Tectonophysics 724-725, 93-115.

Morawiec A (1997) Distributions of misorientation angles and misorientation axes for crystallites with different symmetries. Acta Crystallographica A53, 273-285

Morawiec, A. (1995) Misorientation angle distribution of randomly oriented symmetric objects. Journal of Applied Crystallography 28, 289-293

Obata, M, Ozawa, K. (2011) Topotaxic relationships between spinel and pyroxene in kelyphite after garnet in mantle-derived peridotites and their implications to reaction mechanism and kinetics. Mineralogy and Petrology 101, 217-224, doi:10.1007/s00710-011-0145-y

Plümper, O., King, H.E., Vollmer, C., Ramasse, Q., Jung, H., Austrheim, H. (2012) The legacy of crystal-plastic deformation in olivine - high-diffusivity pathways during serpentinization. Contribution to Mineralogy and Petrology 163 (4), 701–724.

Porter, D.A., Easterling, K.E. (1992). Phase transformations in metals and alloys. Chapmann and Hall

Rosière, C.A., Siemes, H., Quade, H., Brokmeier, H.G., Jansen, E.M. (2001) Microstructures, textures and deformation mechanisms in hematite. Journal of Structural Geology 23, 1429–1440.

Smith, D. (1995) Chlorite-rich ultramafic reaction zones in Colorado Plateau xenoliths: recorders of sub-Moho hydration. Contributions to Mineralogy and Petrology 121, 185–200.

Smith, D. (2010). Antigorite peridotite, metaserpentinite, and other inclusions within diatremes on the Colorado Plateau, SW USA: implications for the mantle wedge during low-angle subduction. Journal of Petrology 51 (6), 1355–1379.

Sutton A.P., Balluffi, R.W. (1995) Interfaces in Crystalline Materials. Clarendon Press, Oxford, UK

Wenk, H.-R., Janssen, C., Kenkmann, T., Dresen, G. (2011) Mechanical twinning in quartz: Shock experiments, impact, pseudotachylites and fault breccias. Tectonophysics 510, 59-79

Wenk HR, Chen K, Smith R (2011) Morphology and microstructure of magnetite and ilmenite inclusions in plagioclase from Adirondack anorthositic gneiss. American Mineralogist 96(8–9):1316–1324

Wheeler, J., Prior, D.J., Jiang, Z., Speiss, R., & Trimby, P.W. (2001). The petrological significance of misorientations between grains. Contributions to Mineralogy and Petrology 141, 109-124.

FIGURE CAPTIONS

Figure 1 – Schematic drawing showing the misorientation between 2 different phases, one "hexagonal" (yellow grain) and a second, "cubic" (purple and green grains). The orientation of the individual crystallites is described by an orientation $\mathbf{g_1}$, $\mathbf{g_2}$ or $\mathbf{g_3}$, which describes the transformation from crystal reference frame (h_i) and sample reference frame (r), here denoted as x,y and z. The misorientation (M) between grains of the same phase can be described as $M=\mathbf{g_2}^{-1}\mathbf{g_3}$, where g are their respective orientations. The misorientation along different phases nevertheless ($M(ip)$ needs to consider the crystallographic system of the individual phases (cs), and can be described like $\boldsymbol{M(ip)}=\mathbf{g_{1(cs1)}}^{-1}\,\mathbf{g_{3(cs2)}}$, where cs_1 is the crystal symmetry of phase 1 (e.g. hexagonal) and cs_2 the crystal symmetry of phase 2 (e.g. cubic). The combined symmetries of the different cs is what defines the dimensions of the fundamental zones for the plots presented here.

Figure 2 – (a) Combined phase and image quality map, showing the distribution of calcite and aragonite. Orientation maps for calcite and aragonite, respectively, inverse pole figure color-coded.

855 **Figure 3** – Pole figures for calcite and aragonite considering all points in the orientation maps from Fig. 2.
856 Scale is given in multiples of uniform distribution. ODFs calculated assuming a halfwidth of 10°.
857
858 **Figure 4** – Interphase misorientation angle (a) and axis (b) distribution for calcite-aragonite, assuming a
859 uniform distribution function, with calcite reference frame plotted in (b). Interphase misorientation angle
860 distribution (c) as calculated from the EBSD orientation map. Red bars on the histogram show the
861 correlated misorientation (between neighbor grains), the orange line shows the uncorrelated distribution
862 calculated from the orientation distribution function, and the yellow line shows the uniform misorientation
863 angle distribution as in (a). Correlated interphase misorientation axis distribution plotted against the
864 calcite reference frame, for all range of misorientation axes from (c). (e) Phase map showing calcite
865 (purple) and aragonite (green), and the more common interphase boundaries traces, with misorientations
866 between adjacent crystals ranging from 30 to 70°. Scales in the pole figures b and d are given in multiples
867 of uniform distribution.
868
869 **Figure 5** – (a) Combined phase and image quality map, showing the distribution of olivine (purple) and
870 antigorite (green), whereas the red phase at the bottom is an isolated grain of magnetite.
871
872 **Figure 6** - Pole figures for olivine and antigorite, considering all points in the orientation maps from Fig.
873 5. Scale is given in multiples of uniform distribution. ODFs calculated assuming a halfwidth of 10°.
874
875 **Figure 7** - Interphase misorientation angle (a) and axis (b) distribution for olivine-antigorite, assuming a
876 uniform distribution function, with olivine reference frame plotted in (b). Interphase misorientation angle
877 distribution (c) as calculated from the EBSD orientation map. Red bars on the histogram show the
878 correlated misorientation (between neighbor grains), the orange line shows the uncorrelated distribution
879 calculated from the misorientation distribution function, and the yellow line shows the uniform
880 misorientation angle distribution as in (a). Correlated interphase misorientation axis distribution (d)

plotted against the olivine reference frame, for misorientations ranging from 70-100°. (e) Image quality map showing the more common interphase boundaries, with misorientations ranging from 70 to 100°. Scales in the pole figures b and d are given in multiples of uniform distribution, phase map is not presented here for better visualization of the interfaces.

Figure 8 - (a) Combined phase and image quality map, showing the distribution of magnetite (purple) and hematite (green).

Figure 9 - Pole figures for magnetite and hematite, considering all points in the orientation maps from Fig. 8. Scale is given in multiples of uniform distribution. ODFs calculated assuming a halfwidth of 10°.

Figure 10 - Interphase misorientation angle (a) and axis (b) distribution for magnetite and hematite, assuming a uniform distribution function, with magnetite reference frame plotted in (b). Interphase misorientation angle distribution (c) as calculated from the EBSD orientation map. Red bars on the histogram show the correlated misorientation (between neighbor grains), the orange line shows the uncorrelated distribution calculated from the misorientation distribution function, and the yellow line shows the uniform misorientation angle distribution as in (a). Correlated interphase misorientation axis distribution (d) plotted against the magnetite reference frame, for misorientations ranging from 20-50°. (e) Image quality (IQ) map showing the most common interphase boundaries traces with misorientations between adjacent grains ranging from 20 to 50°. Scales in the pole figures b and d are given in multiples of uniform distribution, phase map is not presented here for better visualization of the interfaces.

Figure 11 - (a) Combined phase and image quality map, showing the distribution of plagioclase (green), olivine (red) and ilmenite (blue) in the studied gabbro sample. (b) Combined orientation map for plagioclase (IPF color-coded) and image quality for the rest of the phases.

907 **Figure 12** - Pole figures for plagioclase, olivine and ilmenite, considering all points in the orientation
908 maps from Fig. 8. Scale is given in multiples of uniform distribution. ODFs calculated assuming a
909 halfwidth of 10°.
910
911 **Figure 13** - Interphase misorientation angle (a, c) and axis (b, d) distribution for the pairs plagioclase-
912 olivine and plagioclase-ilmenite, respectively, assuming a uniform orientation distribution function. On
913 stereogram (b) plagioclase reference frame is given as black letters in white background, whereas certain
914 olivine directions are given in black background and white letters. The same is valid for the plot (d), but
915 for ilmenite. Scale bars in b and d are given in multiples of uniform distribution.
916
917 **Figure 14** - Interphase misorientation angle distribution (a, c) and axes (b, d) as calculated from the EBSD
918 orientation map, for the pairs plagioclase-olivine and plagioclase-ilmenite, respectively. Red bars on the
919 histogram show the correlated misorientation (between neighbor grains), the orange line shows the
920 uncorrelated distribution calculated from the misorientation distribution function, and the yellow line
921 shows the uniform misorientation angle distribution as in Fig. 13 a,c. On the plot (b) misorientation angles
922 are limited to a range between 65-90° for plagioclase-olivine, whereas in (d) the misorientation range is
923 from 85-130°, for plagioclase-ilmenite pair. On stereogram (b) plagioclase reference frame is given as
924 black letters in white background, whereas certain olivine directions are given in black background and
925 white letters. The same is valid for the plot (d), but for ilmenite. Scale bars in b and d are given in
926 multiples of uniform distribution.
927
928 **Figure 15** – Image quality maps showing plagioclase-olivine interphase boundaries traces with adjacent
929 interphase misorientations ranging from 60-100° misorientation (a) and plagioclase-ilmenite interface
930 traces with misorientation ranging from 60-120°.
931

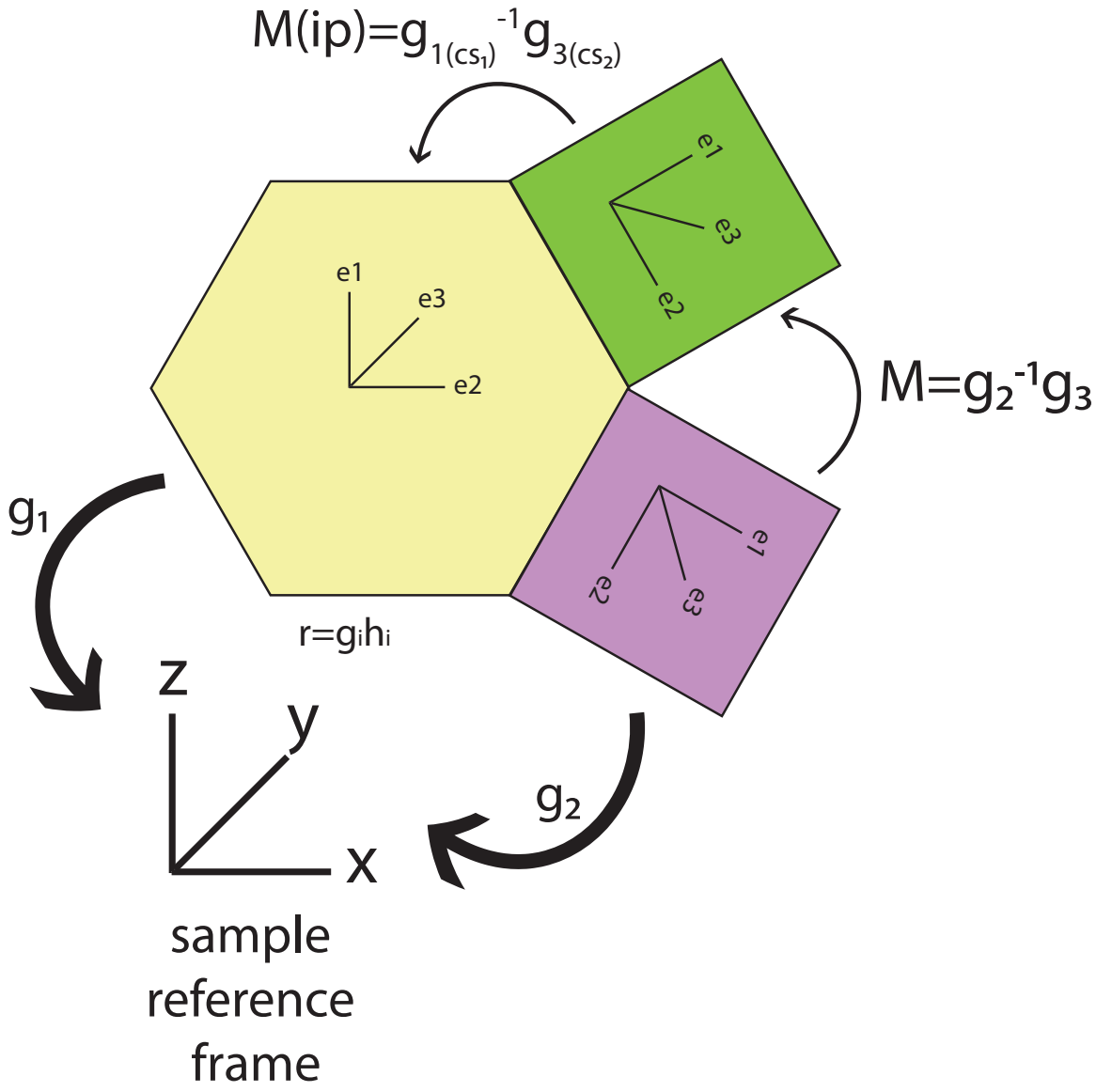
M(ip)=g1(cs1)-1g3(cs2)
e1
e3
e2
M=g2-1g3
g1
r=gihi
z
y
x
g2
sample
reference
frame

Figure 1

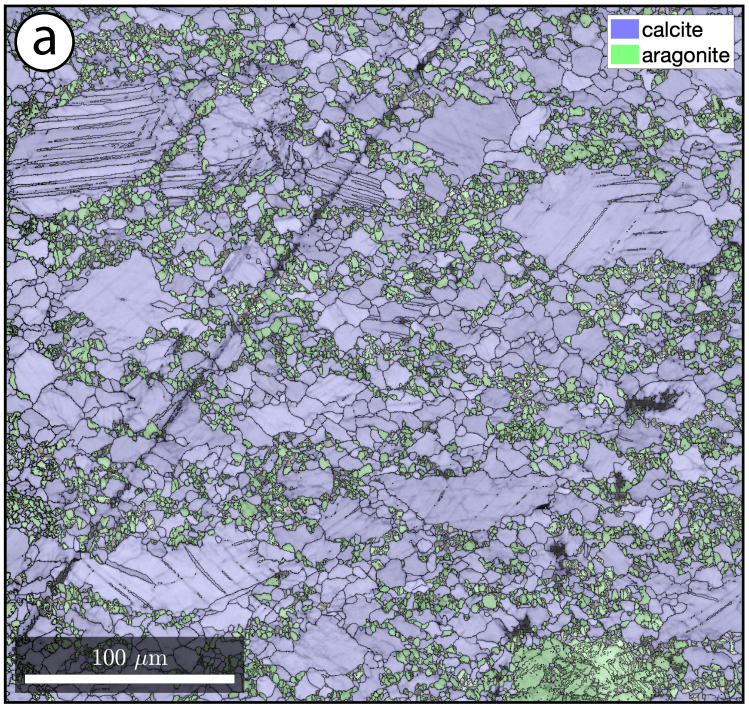
a
calcite
aragonite
100 μm

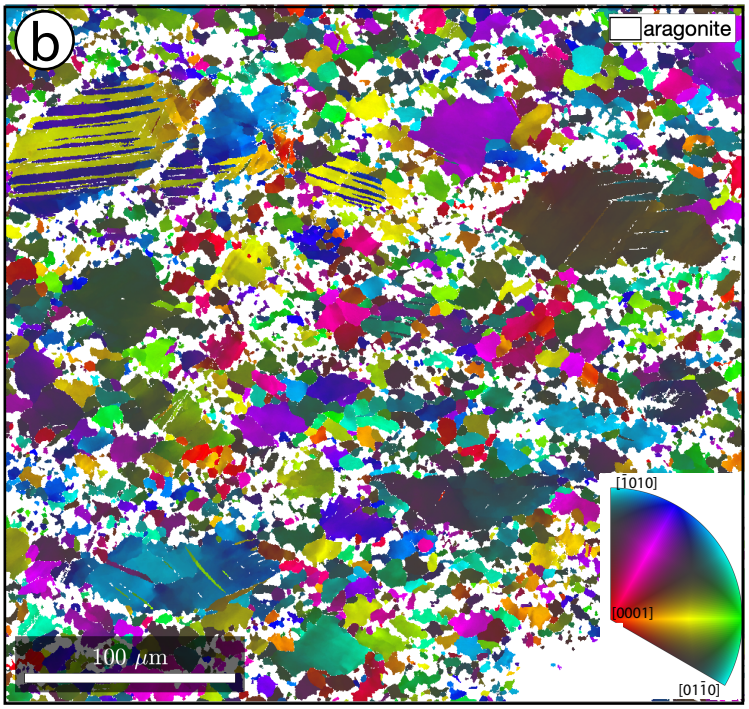
b
aragonite
[$\bar{1}$010]
[0001]
[01$\bar{1}$0]
100 μm

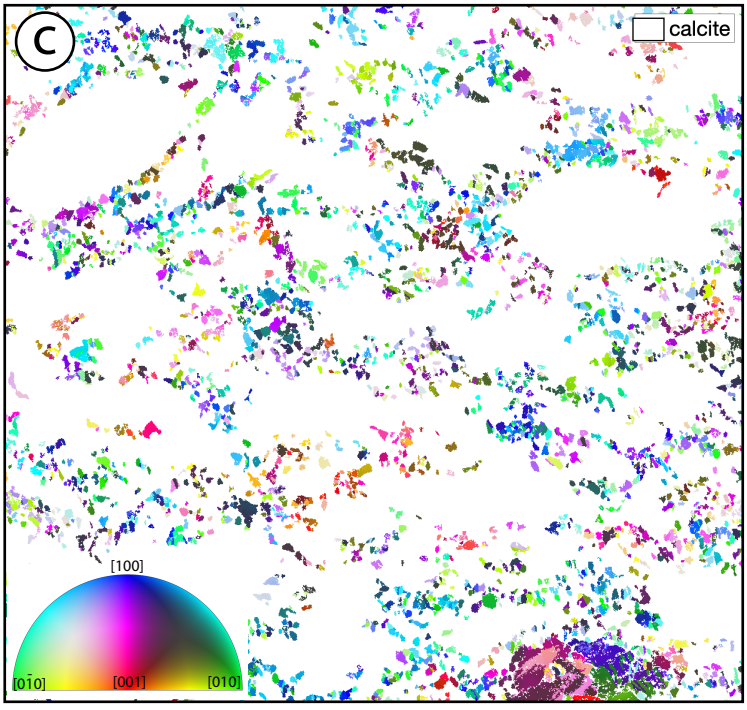
c
calcite
[100]
[0$\bar{1}$0]
[001]
[010]

Figure 2

Calcite pole figures

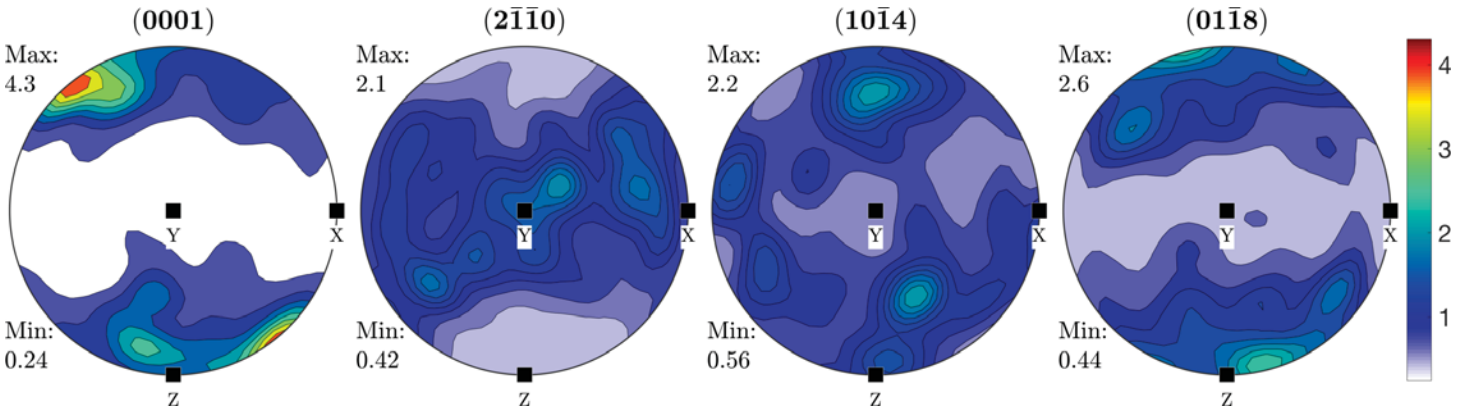

Aragonite pole figures

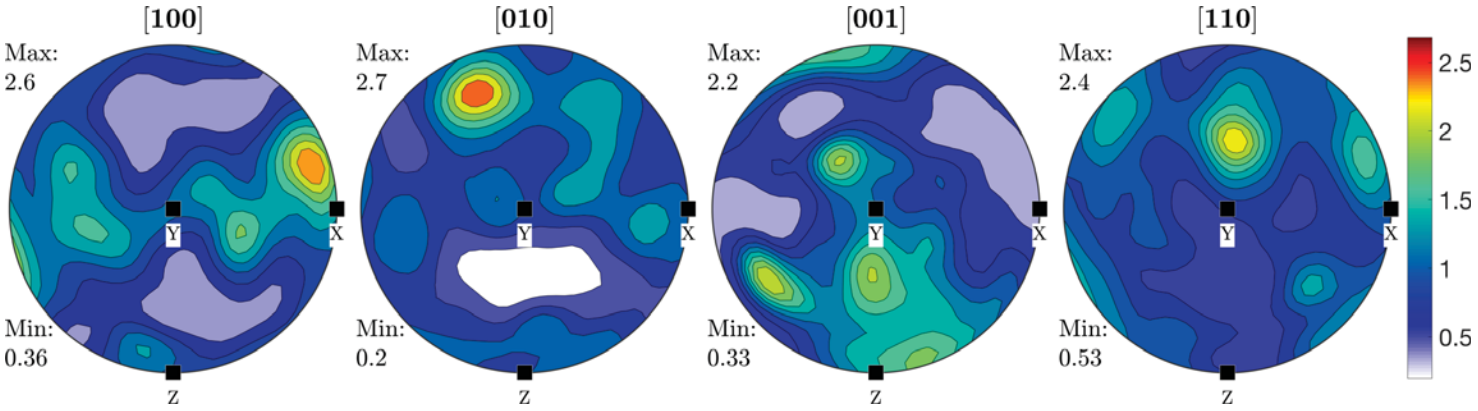

Figure 3

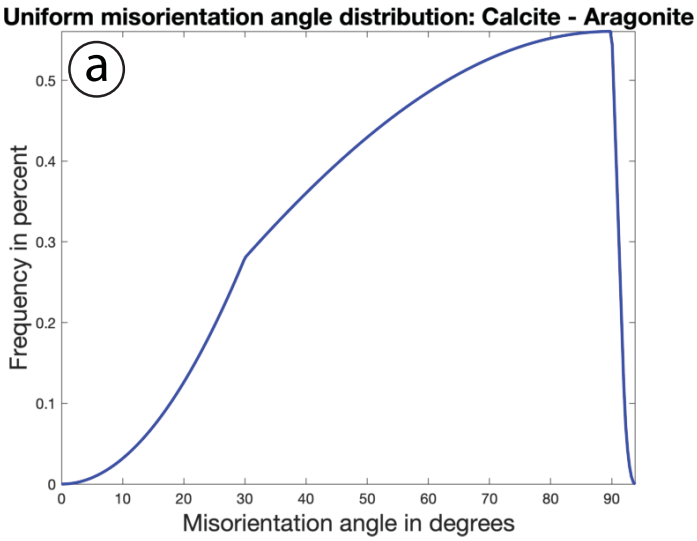
Uniform misorientation angle distribution: Calcite - Aragonite
a
Frequency in percent
Misorientation angle in degrees

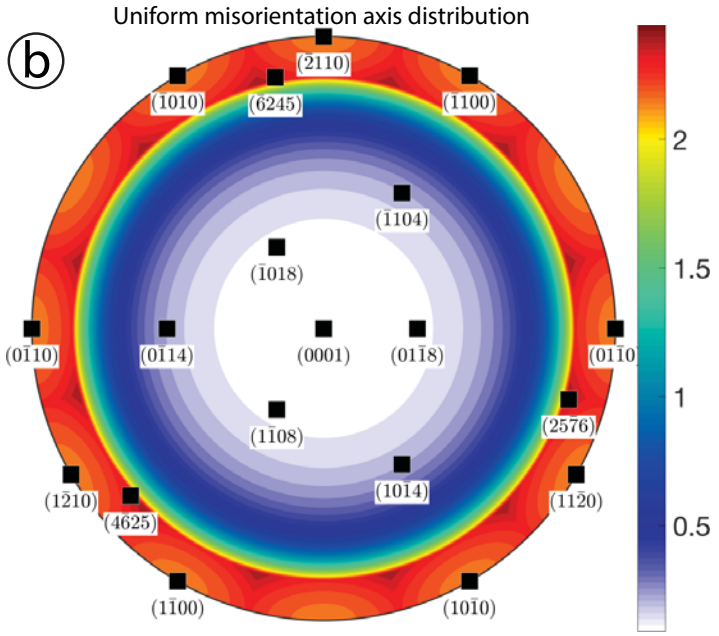
Uniform misorientation axis distribution
b

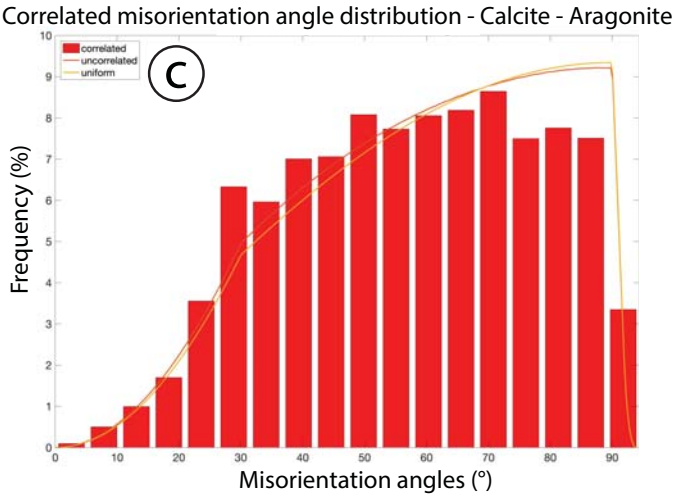
Correlated misorientation angle distribution - Calcite - Aragonite
c
correlated
uncorrelated
uniform
Frequency (%)
Misorientation angles (°)

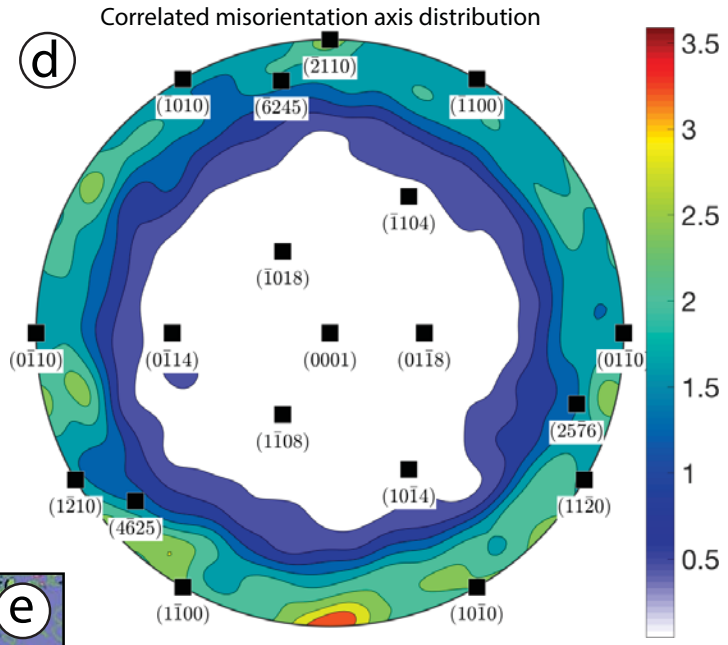
Correlated misorientation axis distribution
d

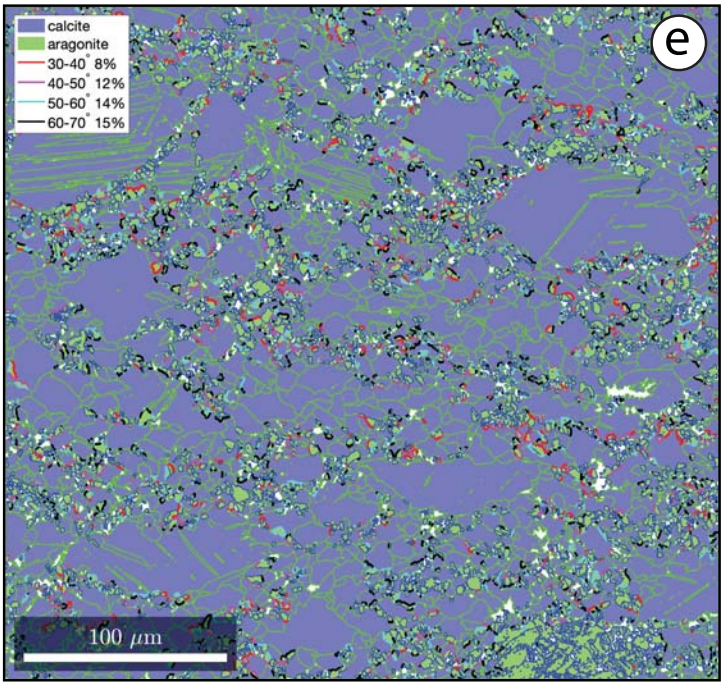
calcite
aragonite
30-40° 8%
40-50° 12%
50-60° 14%
60-70° 15%
e
100 μm

Figure 4

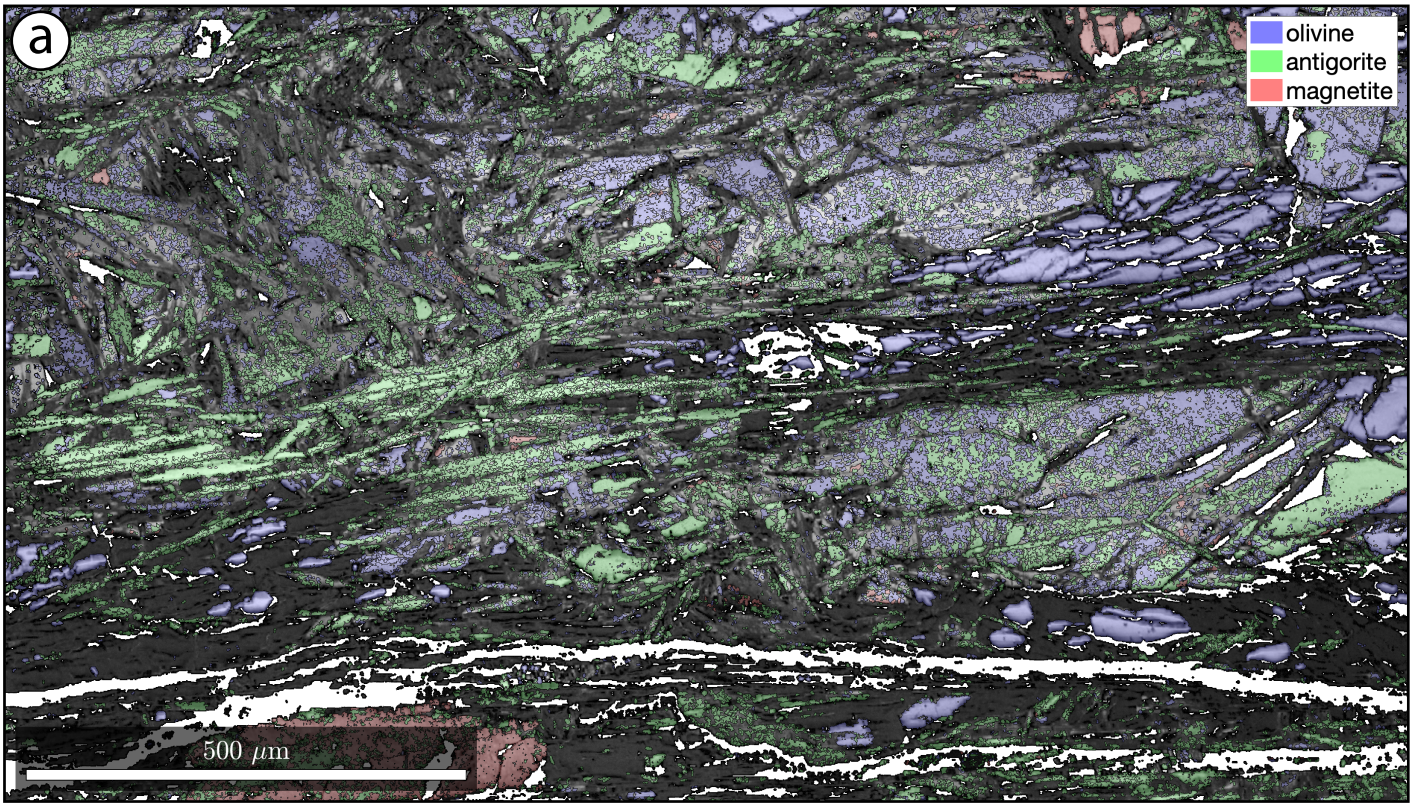

Figure 5

Olivine pole figures

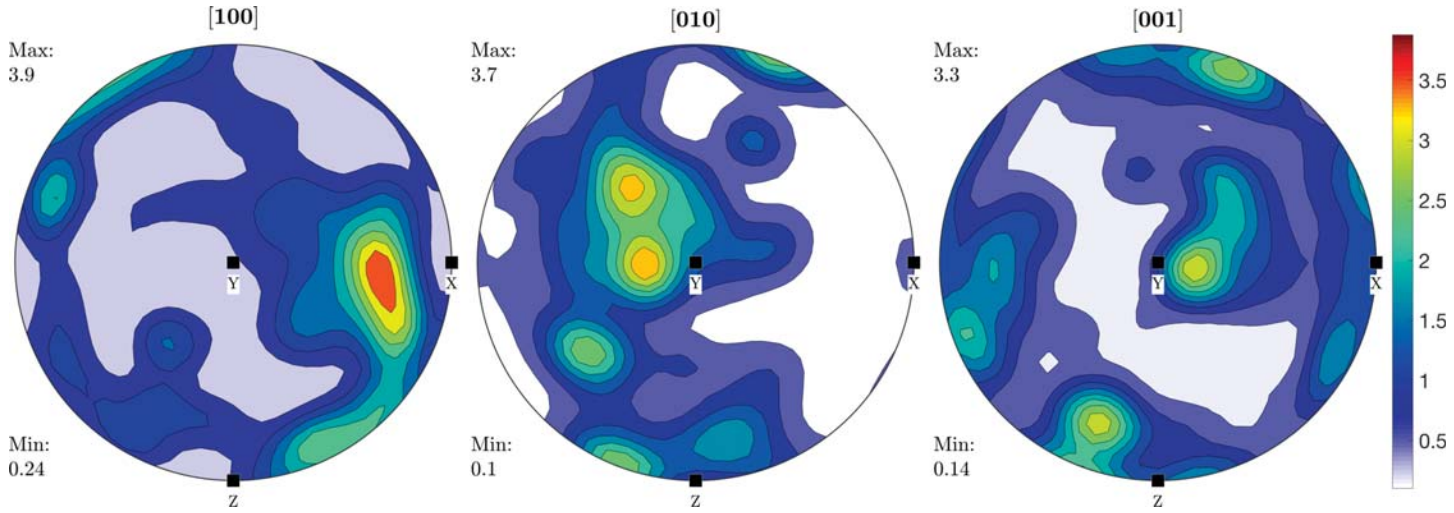

Antigorite pole figures

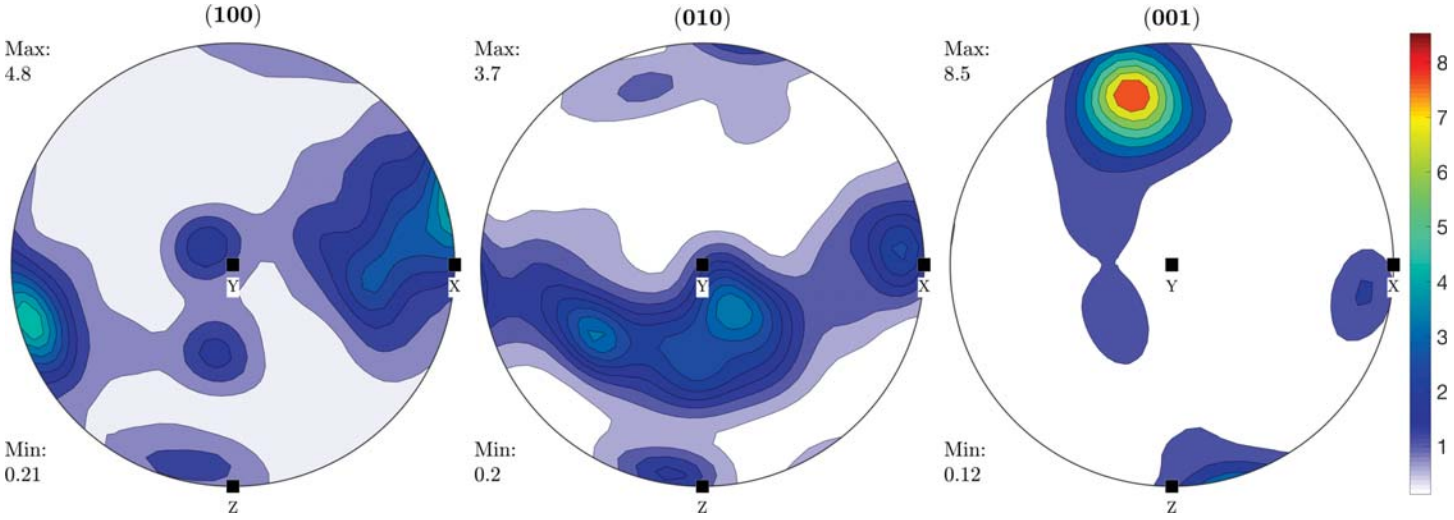

Figure 6

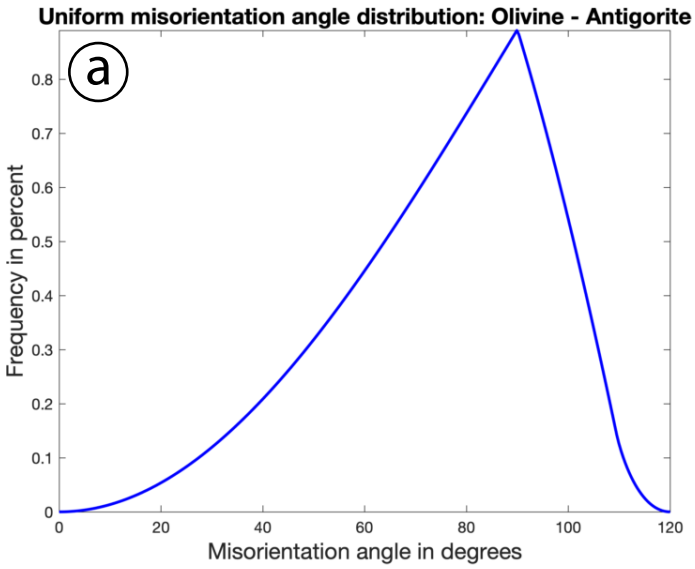
Uniform misorientation angle distribution: Olivine - Antigorite
a
Frequency in percent
Misorientation angle in degrees

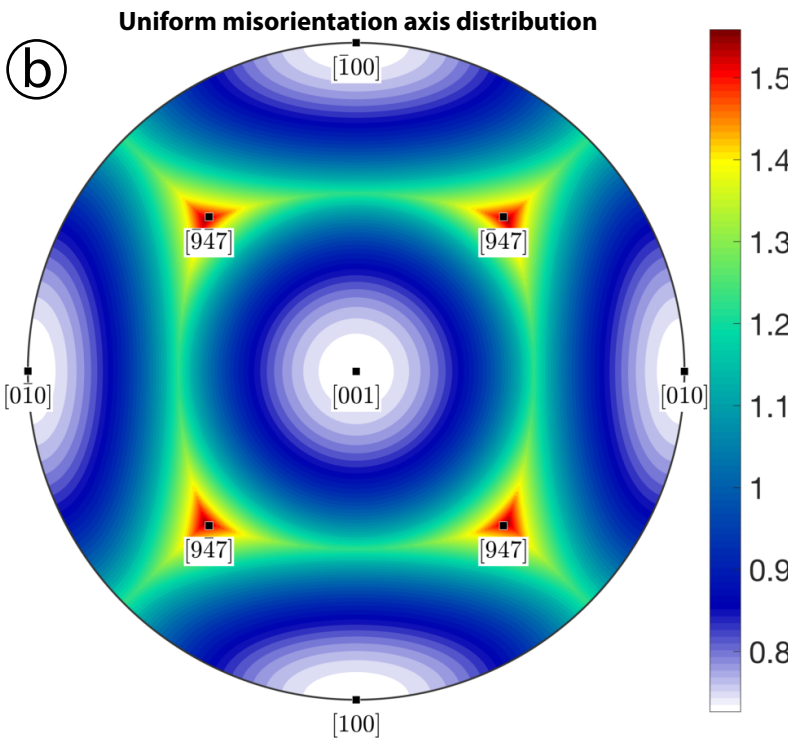
Uniform misorientation axis distribution
b
[1̄00]
[9̄47]
[947]
[010]
[001]
[100]

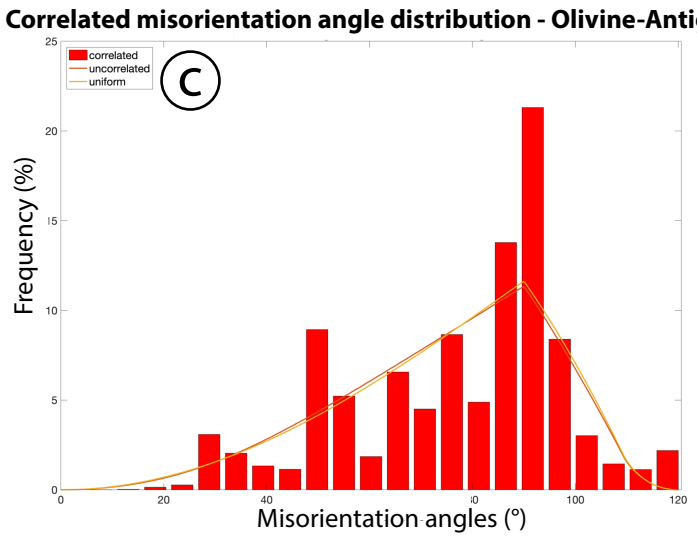
Correlated misorientation angle distribution - Olivine-Antigorite
c
correlated
uncorrelated
uniform
Frequency (%)
Misorientation angles (°)

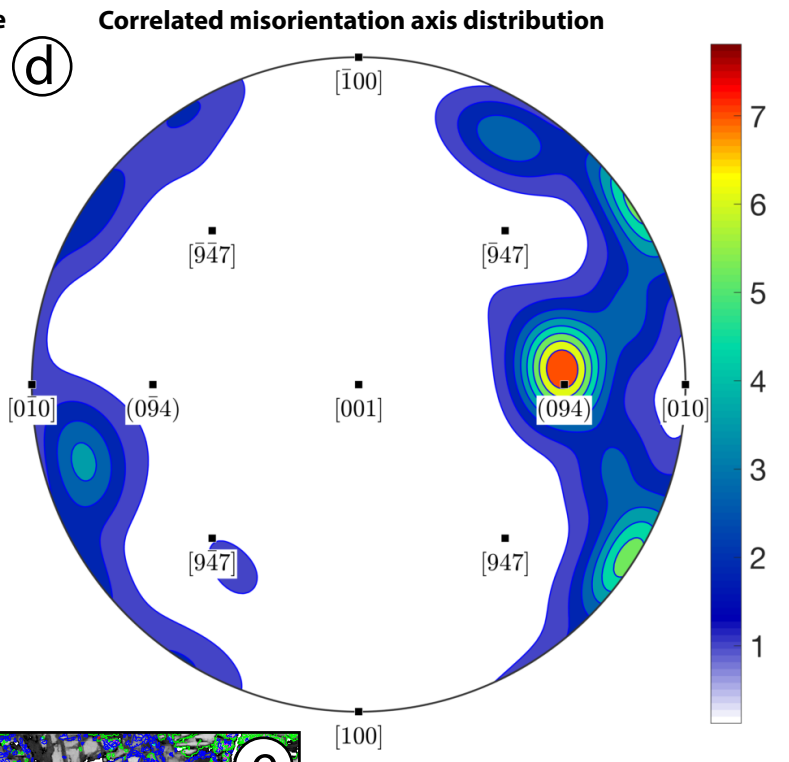
Correlated misorientation axis distribution
d
[1̄00]
[9̄47]
[947]
[010]
(09̄4)
[001]
(094)
[100]

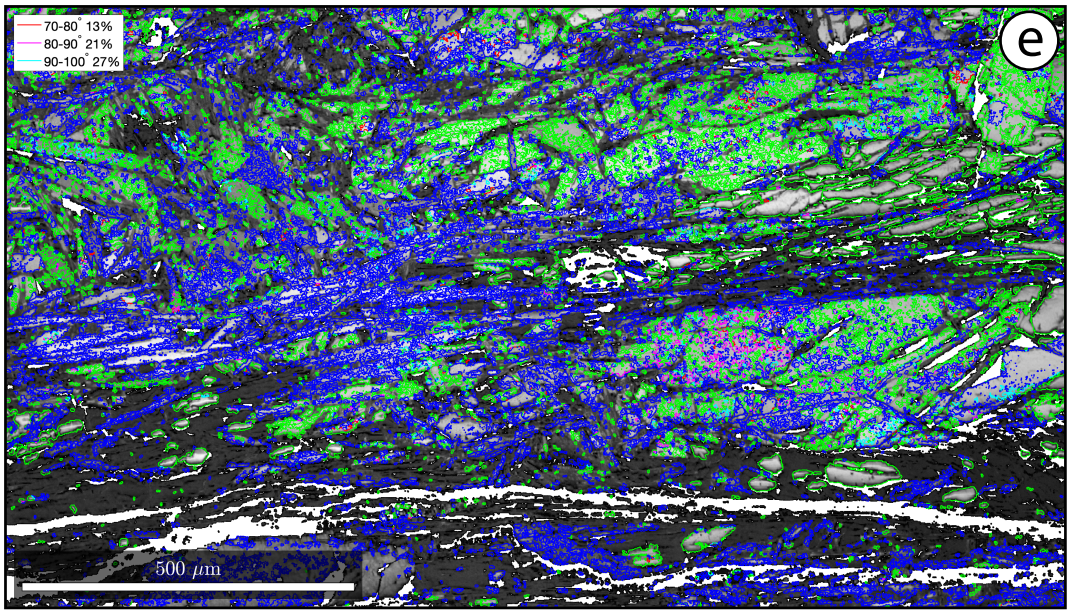
70-80° 13%
80-90° 21%
90-100° 27%
e
500 μm

Figure 7

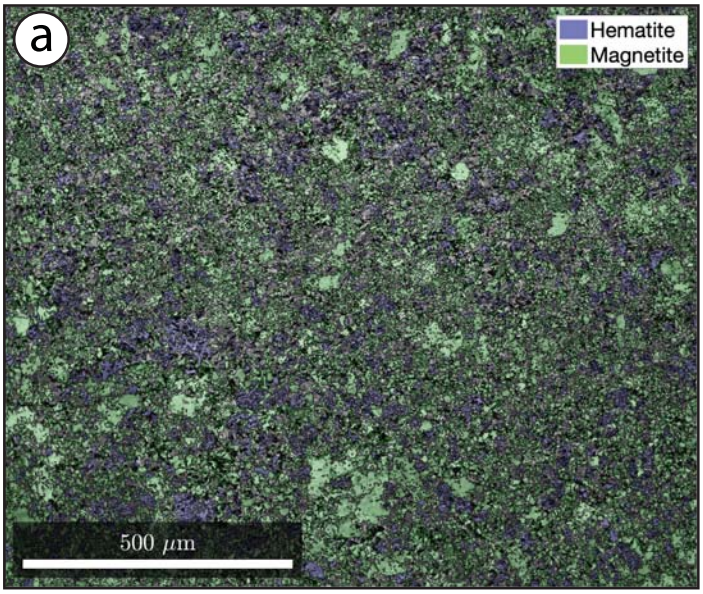

Figure 8

Magnetite pole figures

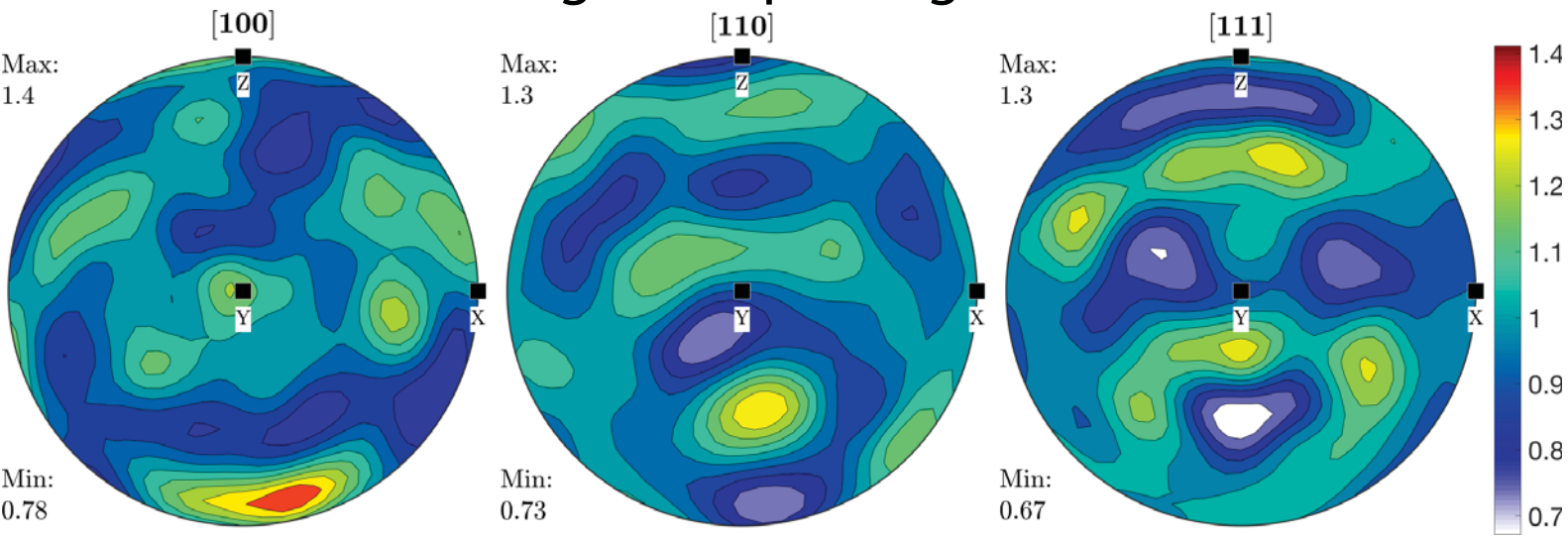

Hematite pole figures

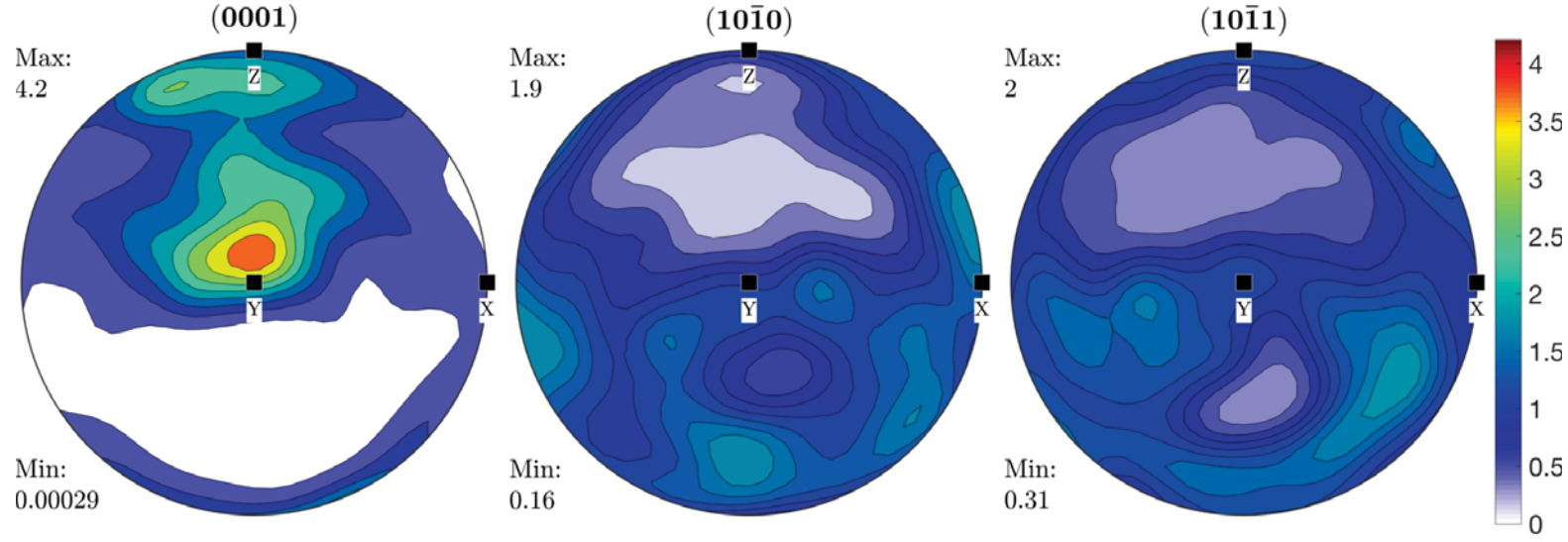

Figure 9

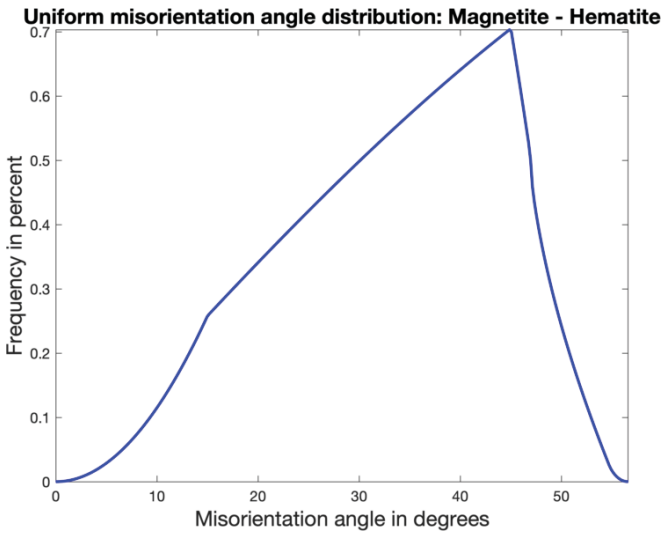
Uniform misorientation angle distribution: Magnetite - Hematite
Frequency in percent
Misorientation angle in degrees
0
0.1
0.2
0.3
0.4
0.5
0.6
0.7
0
10
20
30
40
50

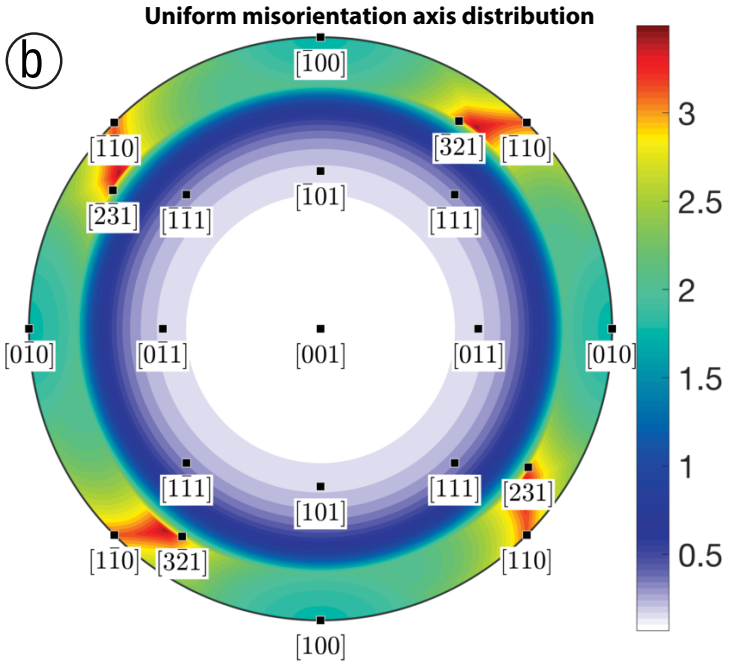
b
Uniform misorientation axis distribution
[100]
[1̄10]
[321]
[110]
[231]
[1̄11]
[101]
[111]
[010]
[01̄1]
[001]
[011]
[010]
[111]
[231]
[101]
[1̄10]
[321]
[110]
[100]
3
2.5
2
1.5
1
0.5

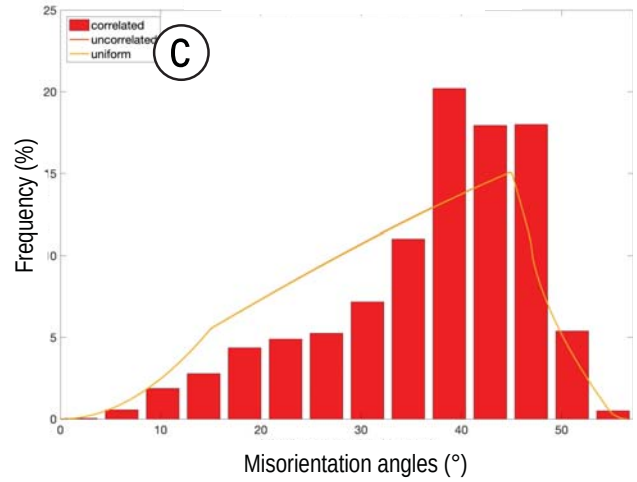
Correlated misorientation angle distribution - Magnetite-hematite
c
correlated
uncorrelated
uniform
Frequency (%)
Misorientation angles (°)
0
5
10
15
20
25
0
10
20
30
40
50

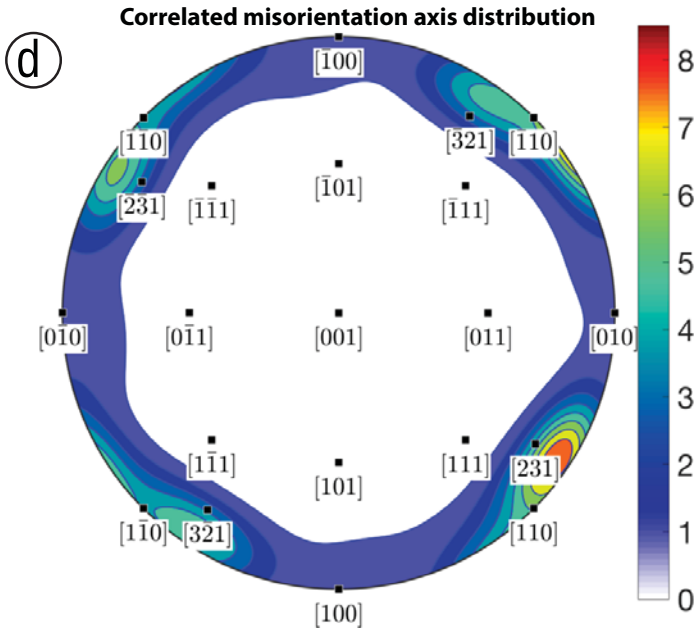
d
Correlated misorientation axis distribution
[100]
[1̄10]
[321]
[110]
[231]
[1̄11]
[101]
[111]
[010]
[01̄1]
[001]
[011]
[010]
[1̄11]
[101]
[111]
[231]
[1̄10]
[321]
[110]
[100]
8
7
6
5
4
3
2
1
0

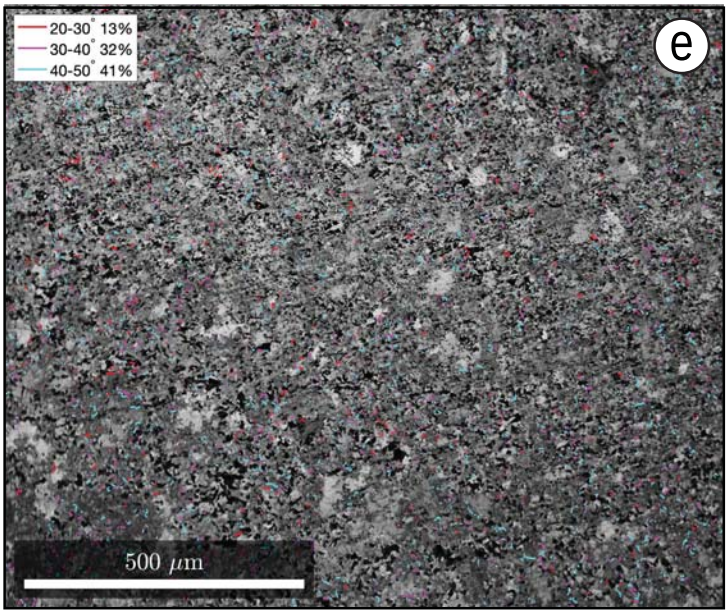
e
20-30° 13%
30-40° 32%
40-50° 41%
500 μm

Figure 10

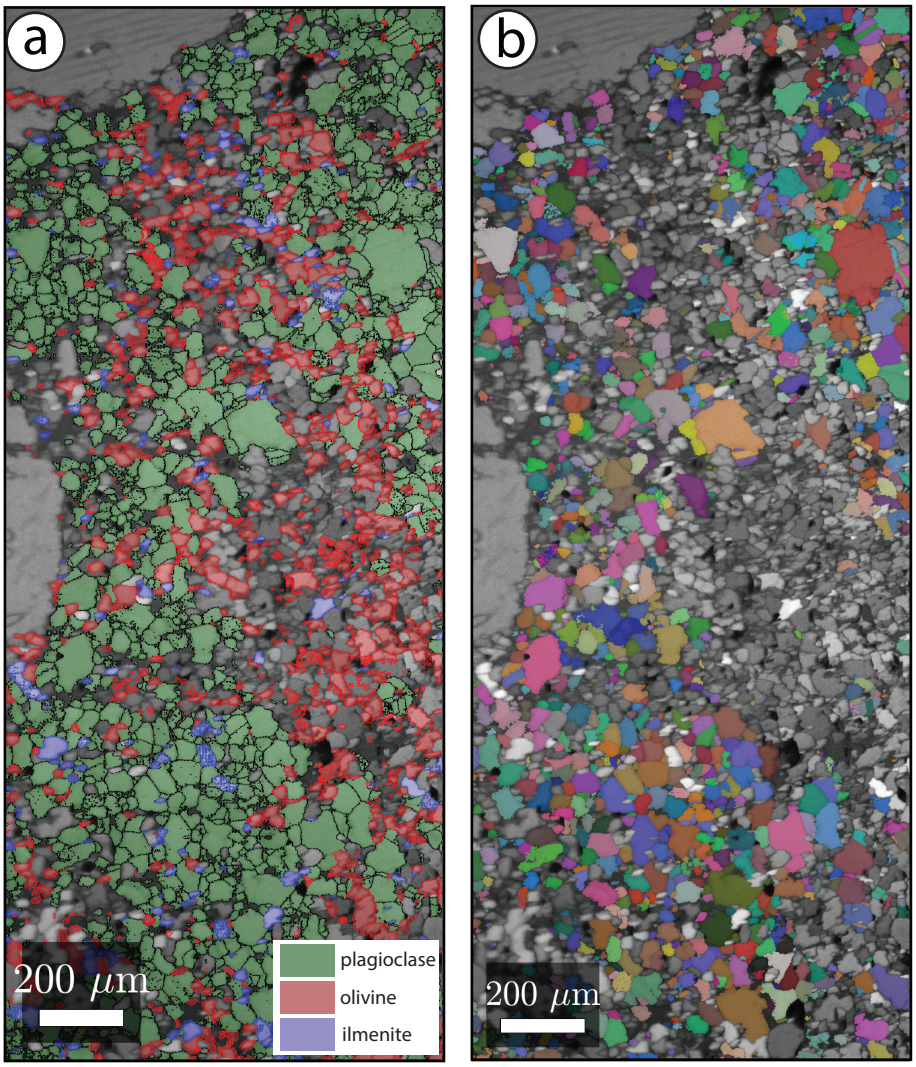

Figure 11

Plagioclase pole figures

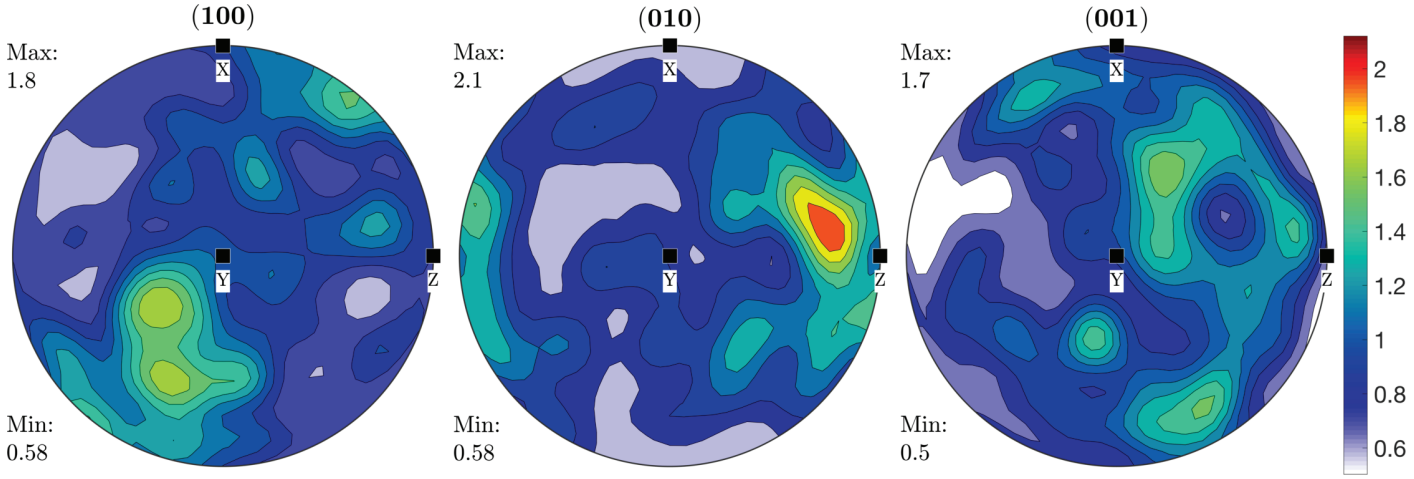

Olivine pole figures

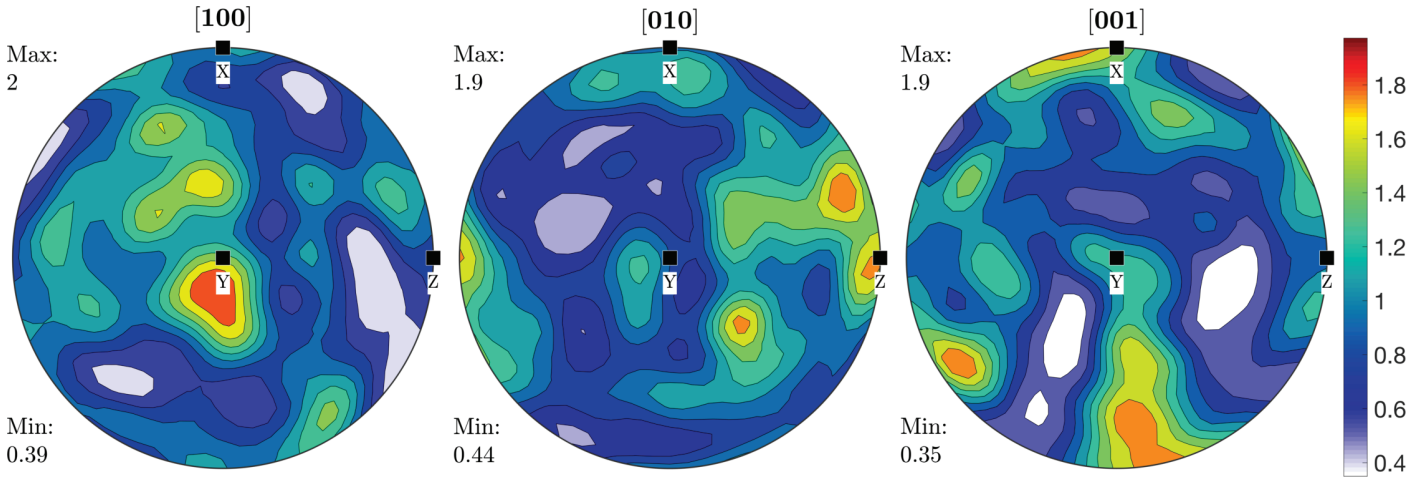

Ilmenite pole figures

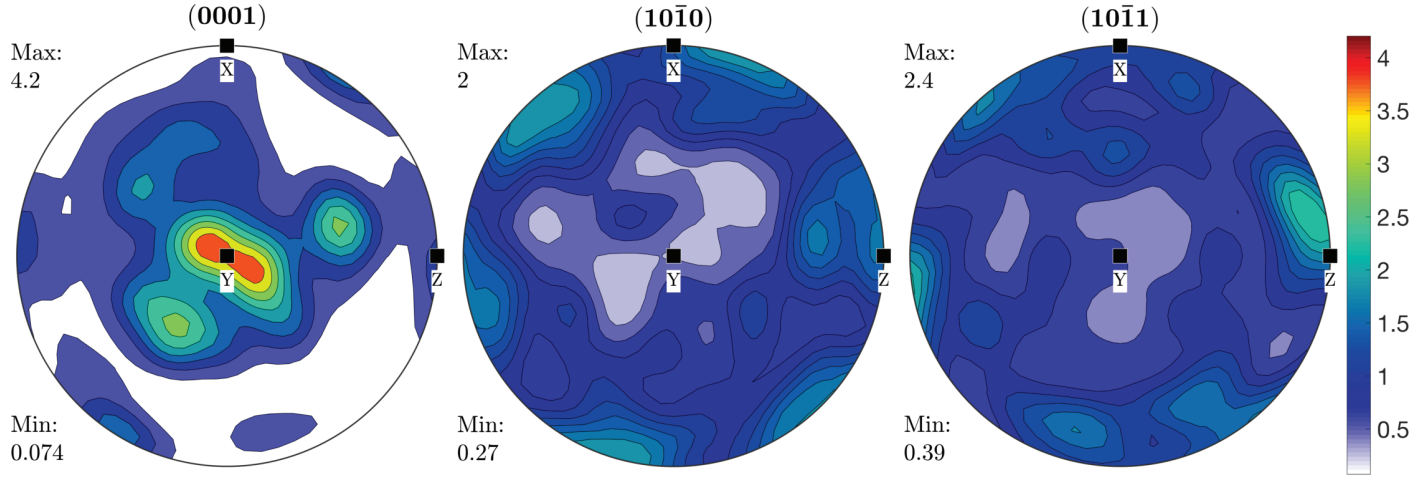

Figure 12

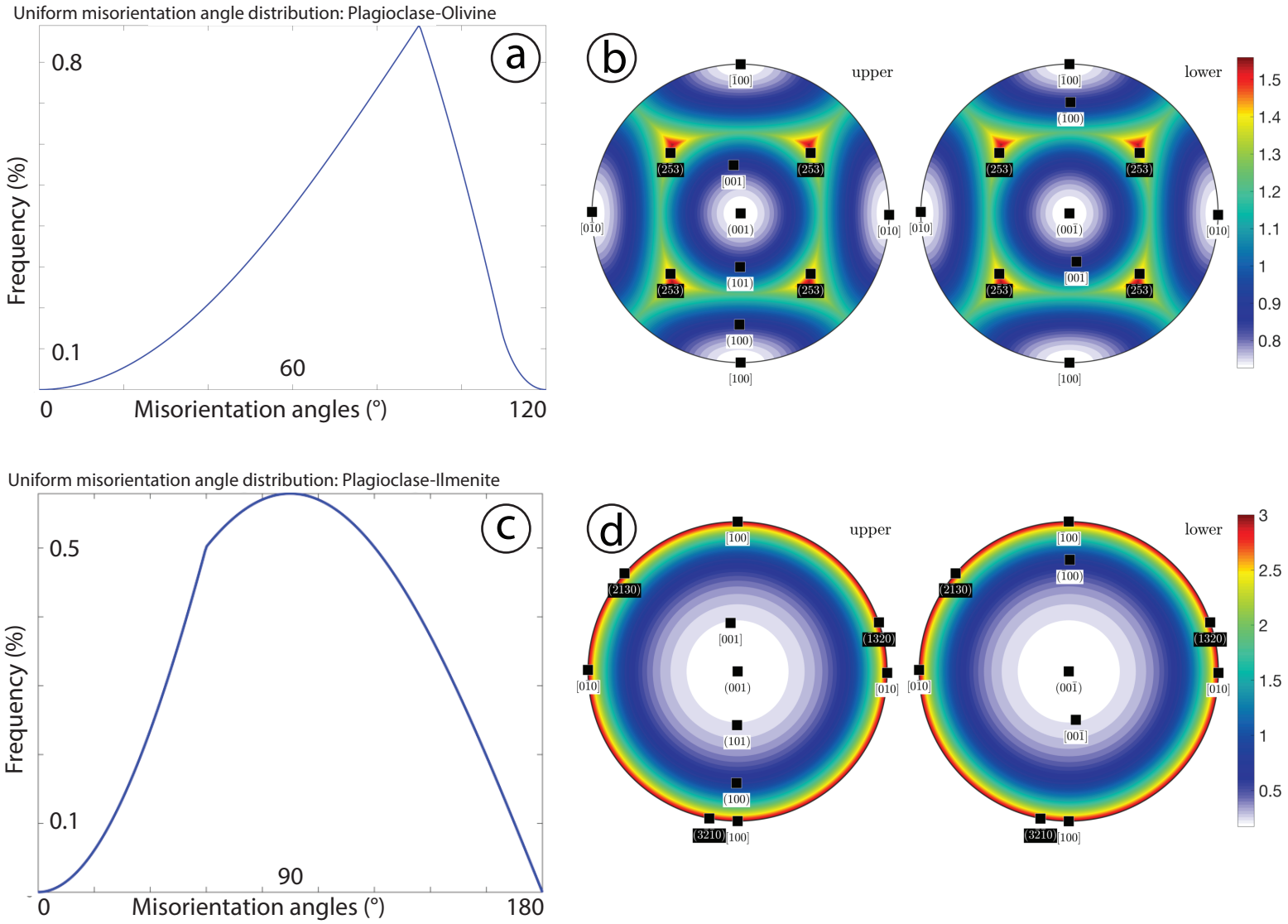
Uniform misorientation angle distribution: Plagioclase-Olivine
a
0.8
0.1
Frequency (%)
60
0
Misorientation angles (°)
120
b
upper
lower
1.5
1.4
1.3
1.2
1.1
1
0.9
0.8
Uniform misorientation angle distribution: Plagioclase-Ilmenite
c
0.5
0.1
Frequency (%)
90
0
Misorientation angles (°)
180
d
upper
lower
3
2.5
2
1.5
1
0.5

Figure 13

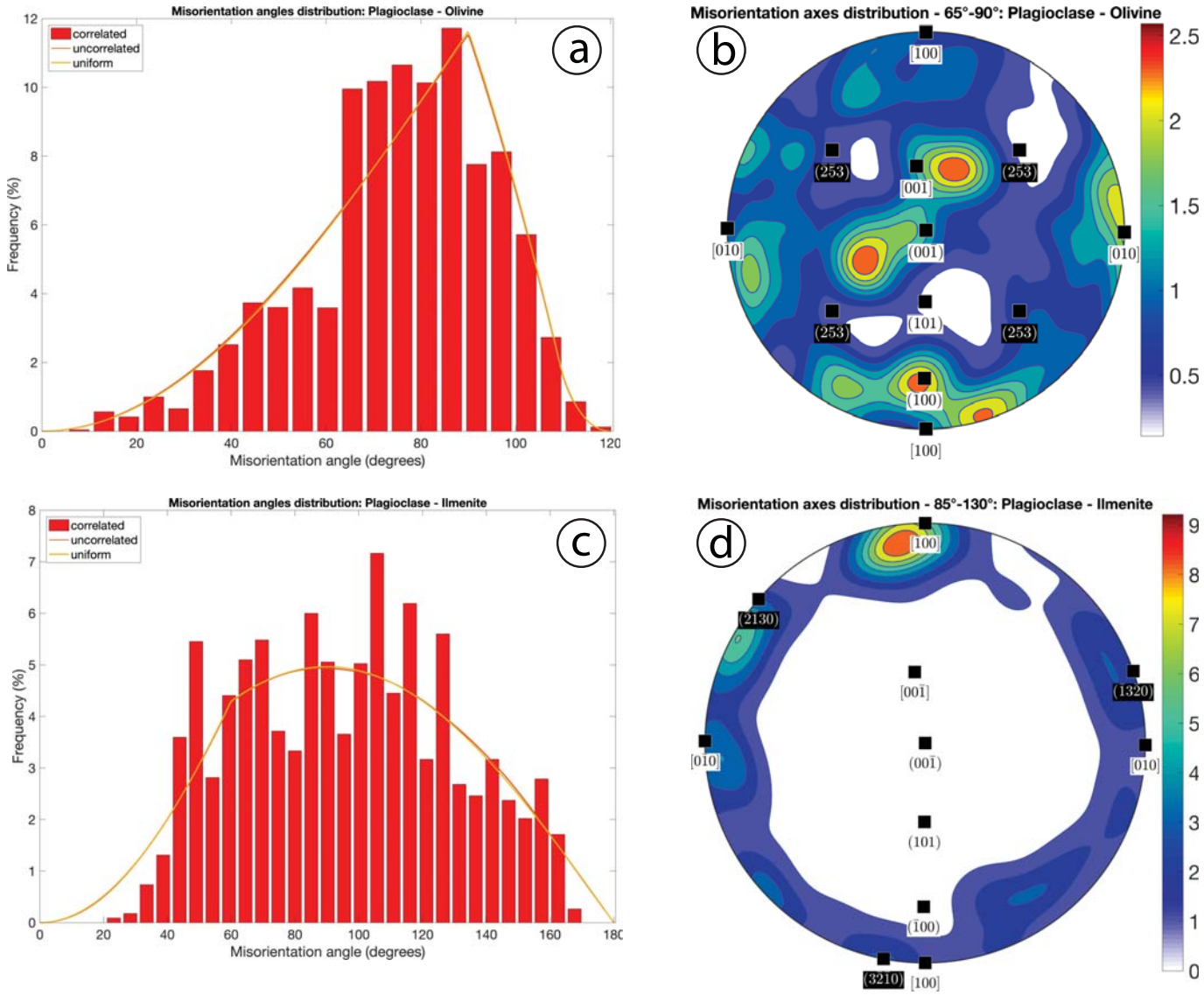
Misorientation angles distribution: Plagioclase - Olivine
correlated
uncorrelated
uniform
a
Frequency (%)
Misorientation angle (degrees)
Misorientation axes distribution - 65°-90°: Plagioclase - Olivine
b
[100]
(253)
[001]
(253)
[010]
(001)
[010]
(253)
(101)
(253)
(100)
[100]
Misorientation angles distribution: Plagioclase - Ilmenite
correlated
uncorrelated
uniform
c
Frequency (%)
Misorientation angle (degrees)
Misorientation axes distribution - 85°-130°: Plagioclase - Ilmenite
d
[100]
(2130)
[00ī]
(1320)
[0ī0]
(00ī)
[010]
(101)
(ī00)
(3210)
[100]

Figure 14

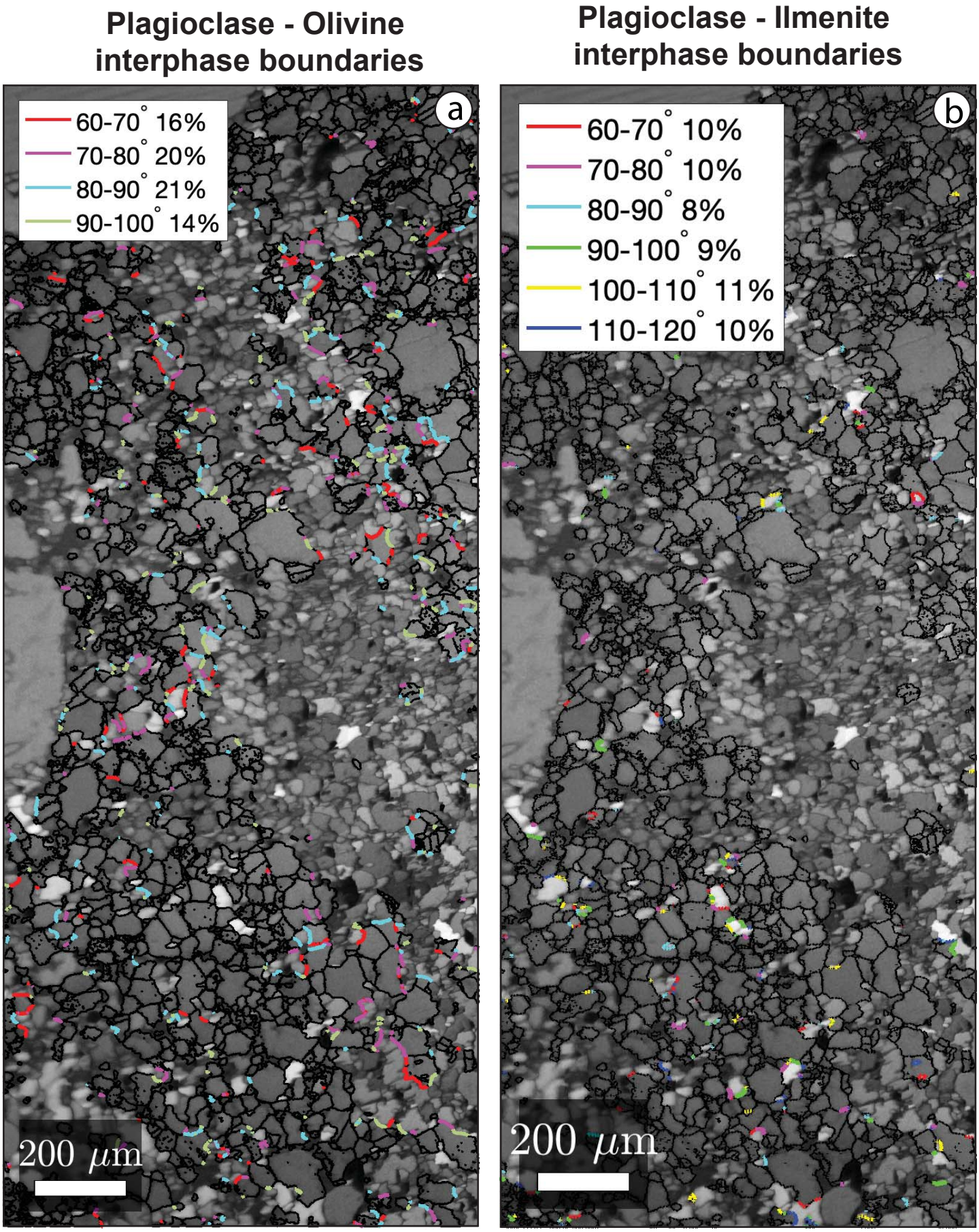
Plagioclase - Olivine
interphase boundaries
60-70° 16%
70-80° 20%
80-90° 21%
90-100° 14%
a
200 μm
Plagioclase - Ilmenite
interphase boundaries
60-70° 10%
70-80° 10%
80-90° 8%
90-100° 9%
100-110° 11%
110-120° 10%
b
200 μm

Figure 15